

Cell-kinetics based calibration of a multiscale model: Application to cell population dynamics in ovarian follicles

B. Aymard^{*†} F. Clément[†] D. Monniaux^{‡§¶} M. Postel^{*†}

August 24, 2015

Abstract

In this work, we present a strategy for tuning the parameters of a multiscale model of structured cell populations in the physiological context of ovulation. We compute different mesoscopic and macroscopic quantities from the microscopic unknowns (cell densities) and relate them to experimental cell kinetic indexes. We expose in details the quantitative specifications established from the available biological knowledge. We study the expression of reaching times corresponding to characteristic transitions in a particle-like reduction of the original model. We make use of this framework to obtain an appropriate initial guess for the parameters and then perform a sequence of optimization steps to finally propose a realistic simulation of the cell populations in a cohort of interacting ovarian follicles.

Introduction

This article deals with the question of the numerical calibration of a multiscale model of cell-structured populations in the physiological context of ovulation. We expose a strategy for tuning the model parameters, based on both the available biological knowledge, and the theoretical and numerical analysis of the model.

The ovulation event is the endpoint of the developmental process undergone by ovarian follicles, which are spheroidal tissular structures composed of somatic cells and sheltering the oocyte (the female gamete). The follicular development is a morpho-dynamical process spanning several months and involving both proliferation and differentiation of the follicular cells, as well as enlargement of the follicle due first to the increase in the number of cell layers and then to the creation and dilatation of a fluid cavity (an antrum) inside

^{*}Sorbonne Universités, UPMC Univ Paris 06, CNRS, UMR 7598, Laboratoire Jacques-Louis Lions, F-75005, Paris, France

[†]Inria Paris-Rocquencourt Research Center, Mycenae Project-Team, Domaine de Voluceau - BP 105, F-78153 Le Chesnay, Cedex, France

[‡]INRA, UMR85 Physiologie de la Reproduction et des Comportements, F-37380 Nouzilly, France

[§]CNRS, UMR7247, F-37380 Nouzilly, France

[¶]Université François Rabelais de Tours, F-37041 Tours, France; IFCE, F-37380 Nouzilly, France

the follicle [18]. During each ovarian cycle, ovulation results in the release of one (in mono-ovulating species) or several (in poly-ovulating species or strains) oocyte(s) competent for subsequent fertilization and embryo development. The number of ovulations is determined during the terminal phase of follicular development, as the issue of a selection process regulated by endocrine loops between the ovaries and hypothalamo-pituitary axis. Hence, the selection of ovulatory follicle(s), and its corollary, the degeneration of the non-selected follicles, caused by the apoptosis of follicular cells, is an original instance of population dynamics coupled with hormonally-controlled cell kinetics.

To describe the terminal stages of follicular development on a cell-kinetics basis and account for the selection process operated amongst follicles, we have developed a multiscale model describing the number of follicular cells as well as their distribution into different cell states (proliferation, differentiation, and possibly apoptosis). The model is formulated as a system of weakly coupled, non conservative transport equations with controlled velocities and source term, where the unknowns are the cell density in each follicle [11, 10]. Even if, in some sense, this model belongs to the class of renewal equations for structured populations such as those described in (chapter 3 of) [22], it owns a number of specificities that render its theoretical and numerical analysis particularly challenging.

In the last ten years, a number of studies have investigated the theoretical and numerical questions raised by this multiscale model. The well-posedness of the model has been established in [27], where the proof of the existence and uniqueness of weak solutions with bounded initial data is based on a fixed-point argument. Optimal control problems related to the ovulatory trajectories were examined in the framework of hybrid optimal control theory [6], while the reachability of final states corresponding to either ovulatory or atretic cases had been studied in the framework of backwards reachable sets [10]. On the numerical ground, the strategy settled to build an efficient and reliable computing environment has combined the design of a finite-volume scheme dealing with the discontinuous coefficients [4], the embedding of this scheme within a dedicated adaptive mesh based on a multi-resolution approach [5], as well as the implementation on parallel architecture [3].

In this study, we take advantage of our computing environment, as well as of our understanding of the model behavior, to address the question of the numerical calibration of the model with respect to given biological specifications. We have to face, a generic, yet unsolved issue in parameter fitting for physiologically-oriented multiscale mathematical models: although quite precise functional knowledge is available on the lower scales, quantitative experimental data are rather available on the higher scales. In our case, the question is how to infer the parameters entering the microscopic functions (on the level of the follicular cells) from mesoscopic (on the level of the individual follicles, i.e. the number of follicular cells) or macroscopic (on the level of the populations of follicles) information.

The resolution of this additional question is needed to fully exploit the model potential in terms of biological interpretation and to enable us to propose different integrative scenarios that would forecast the number of ovulations and chronology of ovulatory events from a given configuration of initial conditions and main parameters. Due to the anchorage of the model formulation within the concepts of cell biology, we also believe that our calibration strategy has a generic interest and could be applied in its principles to other biological situations.

The paper is organized as follows. In the first section, we recall the cell-dynamics based formulation of the multiscale model as weakly-coupled, non conservative transport equations, with space-dependent velocities and explicit accounting for the mitosis event. In the second section, we derive different mesoscopic or macroscopic quantities from the microscopic unknowns (cell densities) and relate them to experimental cell kinetics indexes, paying special attention to the impact of the contrast in the velocities, according to the phases of the cell cycle. In the third section, we introduce a simplified framework with piecewise constant control terms, that allows us to compute rigorously the reaching times of some characteristic transition zones in the computation domain. In the fourth section, we gather all available biological knowledge to build up specifications on the model outputs and derive constraints on some parameter bounds. We explain how to tune the parameters of the model, first in the case of an ovulatory trajectory, and then, in the fifth section, in a situation of selection amongst a cohort of growing follicles. The paper is accompanied by supplemental materials with some additional numerical results, complementary exposition on the derivation of a priori constraints on the parameters, and details on the sequence of steps followed along the numerical calibration of the model.

1 A controlled multiscale model for structured cell populations: formulation and parameterization

In this section, we recall the complete formulation of the multiscale model representing the terminal development of a cohort of ovarian follicles and its control by pituitary hormone FSH (follicle-stimulating hormone). We refer the interested reader to previous biologically-oriented expositions of the model and introduction to the biological bases underlying the formulation of the different functions entering the equations [7, 9, 11, 8]. We just recall here the salient features of the model formulation.

First, to account for the differential (yet not uncoupled) control exerted by FSH onto the commitment of its target follicular cells towards either proliferation or differentiation, we have introduced two structuring variables, the age x and maturity y , hence we have to deal with a 2D equation for each of the (possibly numerous) follicles. Second, to account for the feedback exerted by the follicles onto the pituitary (mediated by the contributions of follicular cells to the secretion of estradiol and inhibin by the ovaries), we have introduced control terms (denoted by $U(t)$ and $u_f(t)$ in the sequel) underlying the interactions between follicles, whose formulation depends on moments of the unknowns. An instance of moment-based control term occurs in the context of hematopoiesis (see e.g. [1]). However, in that case, as in other problems of control of hyperbolic partial differential equations (see e.g. [28]), the control term operates on a boundary, whereas in our case the control variables operate on the velocities and source term. Third, to account for the differences in cell sensitivity to extracellular signals according to the different phases of the cell division cycle [35], we cannot distribute the term representing mitosis (cell doubling) over all cell ages, and we have to tackle discontinuities both in the velocities and density on internal boundaries of the domain representing the passage from one cell phase to another.

We consider a cohort of F interacting follicles. The cell density $(\phi_f(t, x, y))_{f=1, \dots, F}$ within

each follicle satisfies the following system of equations, for $f = 1, \dots, F$:

$$\frac{\partial \phi_f}{\partial t} + \frac{\partial (g_f(x, y, u_f(t)) \phi_f)}{\partial x} + \frac{\partial (h_f(x, y, u_f(t)) \phi_f)}{\partial y} = -\Lambda(x, y, U(t)) \phi_f, \quad (1)$$

set in the computing domain Ω in the (x, y) plane,

$$\Omega = \{(x, y), 0 \leq x \leq N_c \times D_c, 0 \leq y \leq y_{\max}\}$$

where N_c is the number of cell cycles and D_c is the duration of one cycle, and y_{\max} a supremum of the maximum maturity that can be reached by the density. As represented

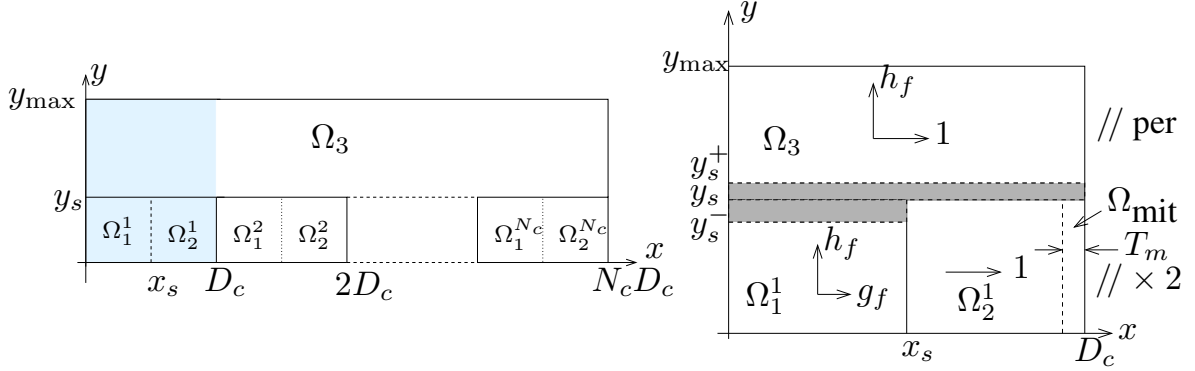


Figure 1: *Left panel: computational domain with the subsequent cell cycles $\Omega_1^p \cup \Omega_2^p$, $p = 1, \dots, N_c$ of length D_c . Ω_1^p corresponds to phase G1, while Ω_2^p aggregates phases S, G2 and M of the p th cell cycle. Phase Ω_3 corresponds to the zone of differentiation, which cells can enter from any Ω_1^p phase. Right panel: single cell cycle, with the different phases G1 (Ω_1^1), SM (Ω_2^1) and D (Ω_3). The part of phase SM corresponding to the mitosis process (Ω_{mit}) is delimited with a dashed line. The zone where cells are sensitive to apoptosis is highlighted in grey. The direction of the aging and maturation velocities are sketched with arrows. Periodic boundary conditions ($//$ per) based on flux continuity are applied on the outer boundaries, with the mitosis-induced density doubling ($// \times 2$) on the vertical boundary at $x = D_c$ for $y \leq y_s$.*

in left panel of Figure 1, the domain Ω is divided in $2N_c + 1$ zones: Ω_1^p, Ω_2^p , for $p = 1, \dots, N_c$ and Ω_3 , corresponding to different cell states and hence different definition of the velocities and source terms. Phase Ω_1^p corresponds to the G1 phase of the cell cycle. Phase Ω_2^p aggregates the three latest phases (S, G2, M) of the p^{th} cell cycle. Phase Ω_3 corresponds to a differentiated state, where cells have exited the cell cycle and undergo terminal differentiation.

$$\begin{cases} \Omega_1^p = \{(x, y) \in \Omega, & pD_c \leq x \leq pD_c + x_s, 0 \leq y \leq y_s\}, p = 0, \dots, N_c - 1, \\ \Omega_2^p = \{(x, y) \in \Omega, & pD_c + x_s \leq x \leq (p + 1)D_c, 0 \leq y \leq y_s\}, p = 0, \dots, N_c - 1, \\ \Omega_3 = \{(x, y) \in \Omega, & y_s \leq y\}, \Theta_1 = \cup_{p=1}^{N_c} \Omega_1^p, \Theta_2 = \cup_{p=1}^{N_c} \Omega_2^p. \end{cases}$$

Each cell cycle consists of the $\Omega_1^p \cup \Omega_2^p$ subdomain and Θ_i for $i = 1, 2$ denotes the disconnected union of the N_c corresponding phases Ω_p^i , for $p = 1, \dots, N_c$.

The initial condition $\phi_f(0, x, y) = \phi_{0f}(x, y)$ is defined by (42) in the Appendix A and it suffices here to say that

$$\text{Supp. } \phi_{0f} = [0, 1] \times [\mu_1, \mu_2] \text{ with } 0 < \mu_1 < \mu_2 < y_s. \quad (2)$$

The aging function g_f appearing in (1) is defined by

$$g_f(x, y, u) = \begin{cases} \gamma_1^f u + \gamma_2^f & \text{for } (x, y) \in \Theta_1 \\ 1 & \text{for } (x, y) \in \Theta_2 \cup \Omega_3 \end{cases} \quad (3)$$

where γ_1^f, γ_2^f are real positive constants. The aging velocity g_f modulates the transit time along phase $G1$ and its relative duration with respect to the total cell cycle duration D_c . Hence, even if phase G_1 is assumed to have a different duration than the remaining of the cycle (phase SM), we can set x_s to $D_c/2$ without loss of generality ; the lengths of G_1 and SM will be the same on the domain, but their relative duration will be dynamically settled by the aging function and the choice of its parameter values. In practice, we deal with a phase G_1 longer than SM , so that the aging velocity will be lower than 1.

The maturation function h_f is defined by

$$h_f(x, y, u) = \begin{cases} \tau_h^f(-y^2 + (c_1^f y + c_2^f)(1 - \exp(\frac{-u}{\bar{u}^f}))) & \text{for } (x, y) \in \Theta_1 \cup \Omega_3 \\ 0 & \text{for } (x, y) \in \Theta_2 \end{cases} \quad (4)$$

where τ_h^f, c_1^f, c_2^f and \bar{u}^f are real positive constants. An important feature of $h_f(x, y, u)$ is that for fixed u , it possesses only one strictly positive root in y , and this root remains below a maximal threshold as the value of u increases. Let us denote

$$\theta(u) = 1 - \exp\left(-\frac{u}{\bar{u}^f}\right), \quad \theta(0) = 0, \text{ and } \lim_{u \rightarrow \infty} \theta(u) = 1.$$

The roots of h_f read:

$$\begin{aligned} r_1(u) &= \frac{1}{2} \left(c_1^f \theta(u) - \sqrt{(c_1^f \theta(u))^2 + 4c_2^f \theta(u)} \right), \\ r_2(u) &= \frac{1}{2} \left(c_1^f \theta(u) + \sqrt{(c_1^f \theta(u))^2 + 4c_2^f \theta(u)} \right). \end{aligned}$$

It is easy to check that $r_2(u)$ increases with u :

$$r_2(0) = 0 \text{ and } \lim_{u \rightarrow \infty} r_2(u) = \frac{1}{2} \left(c_1^f + \sqrt{c_1^{f2} + 4c_2^f} \right). \quad (5)$$

The source term, that represents cell loss through apoptosis, is defined by

$$\Lambda(x, y, U) = \begin{cases} \bar{\Lambda} \exp\left(-\left(\frac{y - y_s}{\bar{y}}\right)^2\right) \times \frac{U_{\max} - U}{U_{\max}} \mathbb{1}_{[y_s^-, y_s^+]} & \text{for } (x, y) \in \Theta_1 \cup \Omega_3 \\ 0 & \text{for } (x, y) \in \Theta_2 \end{cases} \quad (6)$$

where $\bar{\Lambda}, y_s$ and \bar{y} are real positive constants. $\Lambda(x, y, U)$ is nonzero only in a restricted range $y \in [y_s^-, y_s^+]$ with $0 < y_s^- < y_s < y_s^+ < y_{\max}$, while its maximal value is reached

when both U takes its lowest value U_{\min} (penalization due to poor hormonal supply), and $y = y_s$ (highest sensitivity to apoptosis at the cell cycle exit transition).

The F equations in the PDE system (1) are linked together through the arguments $u_f(t)$, appearing in the velocities $g_f(x, y, u)$ and $h_f(x, y, u)$, and $U(t)$, appearing in the source term $\Lambda(x, y, U)$, which depend on the first maturity moment of the densities

$$\begin{aligned} m_f^1(t) &= \int_0^1 \int_0^{N_c D_c} y \phi_f(t, x, y) dx dy \\ M(t) &= \sum_{f=1}^F m_f^1(t). \end{aligned} \quad (7)$$

The plasma FSH level $U(t)$ showing up in the arguments of the source term in (1) is defined by

$$\begin{aligned} U(t) &= S(M(t)) \\ \text{with } S(M) &= U_{\min} + \frac{U_{\max} - U_{\min}}{(1 + \exp(c(M - \bar{M}))^\delta)} \end{aligned} \quad (8)$$

where U_{\min} , U_{\max} , c , δ and \bar{M} are real positive constants.

The locally bioavailable FSH level $u_f(t)$ showing up in the arguments of the velocities in (1) is defined by

$$\begin{aligned} u_f(t) &= b_f(m_f^1(t))U(t) \quad \text{for } f = 1, \dots, F, \\ \text{with } b_f(m) &= b_1^f + \frac{1 - b_1^f}{1 + \exp(-b_2^f(m - b_3^f))}, \end{aligned} \quad (9)$$

where b_1^f , b_2^f and b_3^f are real positive constants. The sigmoid shapes of $S(M)$ and $b_f(m)$ ensure altogether that the mesoscopic control u_f is bounded

$$b_1^f U_{\min} \leq u_f(t) \leq U_{\max}. \quad (10)$$

To alleviate the notations, we drop from now on the upper index f in the constants γ_1^f , γ_2^f , τ_h^f , c_1^f , c_2^f , \bar{u}^f , b_1^f , b_2^f and b_3^f , which indicates that they can vary from one follicle to another. The follicle-dependent character of these parameters will be reminded in the sequel by the f index in functions g_f , h_f and u_f .

The precise definition of the required transmission conditions along the successive cell cycles of the domain has been formulated in [27]. For each cycle $p = 1, \dots, N_c$,

- the flux on the x -axis is continuous on the interface between Ω_1^p and Ω_2^p , for all $p = 1, \dots, N_c$

$$\phi_f(t, x^+, y) = (\gamma_1 u_f + \gamma_2) \phi_f(t, x^-, y), \quad x = pD_c - x_s, \quad 0 \leq y \leq y_s. \quad (11)$$

- The flux is doubling on the interface between Ω_2^p and Ω_1^{p+1} , which accounts for the birth of two daughter cells from one mother cell (mitosis) at the end of each cell cycle, for all $p = 1, \dots, N_c - 1$

$$(\gamma_1 u_f + \gamma_2) \phi_f(t, x^+, y) = 2 \phi_f(t, x^-, y), \quad x = pD_c, \quad 0 \leq y \leq y_s \quad (12)$$

- A homogeneous Dirichlet condition holds to the north of the interface between Ω_2^p and Ω_3

$$\phi_f(t, x, y_s^+) = 0, \quad pD_c - x_s \leq x \leq pD_c. \quad (13)$$

We now comment on the outer boundaries of the computing domain. From (5) and (10), we can see that the maturation velocity in the y direction vanishes at some ordinate lying below a supremum $r_2(U_{\max})$ and above an infimum $r_2(b_1U_{\min})$. Choosing μ_2, c_1, c_2 such that

$$\mu_2 \leq y_s < r_2(b_1U_{\min}) \text{ and } \frac{1}{2} \left(c_1 + \sqrt{c_1^2 + 4c_2} \right) < y_{\max}$$

ensures that $h_f(y, \cdot)$ is strictly positive until above y_s and negative before reaching y_{\max} , so that the density remains null on these two boundaries at all times. This enables us to use periodic boundary conditions in the numerical implementation (see [3]).

In the age variable x , the velocity is always strictly positive, therefore the number of cell cycles N_c can be tuned so as to cover, in as much as possible, the expected time horizon of the simulation, so that no cell may reach the right outer boundary before the end of the simulation. However, to guarantee that the numerical problem be well defined in all cases, we also set boundary conditions on the vertical outer boundaries of the domain:

$$(\gamma_1 u_f + \gamma_2) \phi_f(t, 0^+, y) = 2\phi_f(t, N_c D_c^-, y), \quad x = pD_c, \quad 0 \leq y \leq y_s. \quad (14)$$

Combined with a choice of a sufficiently large N_c , condition (14) still allows one to follow the motion and spreading of the density over successive cycles on the unrolled domain (left panel Figure 1) for a while. Once the condition becomes active, the density reaching the right end on the domain folds itself and starts again from the left end of the domain. In that case, one can continue to track the cell ages, modulo $N_c D_c$. Alternatively, for the sake of computational purposes, condition (14) can be combined with a single cell cycle domain (right panel Figure 1). In that case, the dynamics remain globally unchanged, and the cell age still remains informative on the cell progression along the cycle, but it is no more possible to follow the absolute cell age, since it is reset at the beginning of the cycle, neither the generation lineage of cells.

2 Model outputs on the microscopic, mesoscopic and macroscopic scales

2.1 Macro and mesoscopic moments and derived quantities

From the previous section, it is already clear that the model outputs can span several space scales, from the microscopic scale of the local cell density to the macroscopic scale of moments computed over the whole domain Ω . In this section, we focus on the model outputs that can be directly related to observable variables in the field of experimental cell kinetics. While, as we will see, the total cell number, growth fraction and cell distribution in cytologic ages can be computed straightforwardly, it is not the case of the mitotic index, whose computation principles will be developed in more detail.

The total cell number, that can be assessed from sampled countings [32], is simply the zero-order moment of the density in both age and maturity $m_f^0(t)$

$$m_f^0(t) = \iint_{\Omega} \phi_f(t, x, y) dx dy. \quad (15)$$

Another interesting number is that of the cells lying within the proliferating part of the domain, Ω_1^p, Ω_2^p , for $p = 1, \dots, N_c$, that can also be simply denoted as $\Omega \setminus \Omega_3$. This number allows us to introduce the growth fraction GF , which is the proportion of proliferating cells amongst the whole population. The growth fraction can be assessed by means of cell labeling protocols that detect the passages of cell throughout the S phase of DNA replication [17, 23].

$$GF(t) = \frac{\iint_{\Omega \setminus \Omega_3} \phi_f(t, x, y) dx dy}{\iint_{\Omega} \phi_f(t, x, y) dx dy}. \quad (16)$$

To follow the progression of cells along the cell cycle in more detail, we can also compute the distribution in age within the proliferative part of the domain $\psi(t, x)$ (we drop the f index to simplify notations). This distribution notably gives information about the degree of between-cells synchronization. For instance, a fully desynchronized cell population with $GF=1$ will be distributed according to an exponential distribution with twice as many “young” cells (that have just entered the G1 phase after mitosis) as “old” cells (that are about to divide at the end of the mitosis phase) [2].

$$\psi(t, x) = \int_{\Omega \setminus \Omega_3} \phi_f(t, x, y) dy$$

Another experimental marker is the mitotic index (MI), which assesses the proportion of cells undergoing mitosis [33, 34]. For the sake of concision, we will expose the principles of MI computation from the age distribution $\psi(x, t)$ and express the MI as the proportion of mitotic cells within the population of proliferating cells

$$MI(t) = \frac{\iint_{\Omega_{mit}} \phi_f(t, x, y) dx dy}{\iint_{\Omega \setminus \Omega_3} \phi_f(t, x, y) dx dy}. \quad (17)$$

Expression with respect to the total cell population can be simply obtained by multiplying the MI value by the growth fraction defined in (16). In the model, the mitosis phase is embedded within the SM phase, but we can nevertheless delimit a subpart of the SM phase corresponding specifically to mitosis (Ω_{mit} in right panel of Figure 1). Since the aging velocity is constant in phase SM, and equals 1 (the cell age evolves as time), the relative length of the M phase subpart within the SM phase can be deduced from the relative duration of mitosis T_m (on the order of 30 min) with respect to the whole duration of the SM phase T_{SM} (on the order of 8 hours [13]). We refer the reader to the Appendix A for the computation of the MI in the fully proliferating case. In Appendix A.1 we recover the well known (see [29]) explicit formula $MI(t) = 2^{T_m/D_c} - 1$ in the case of a

constant velocity while in Appendix A.2 we describe a recursive computation in the case of a space dependent velocity. In both situations cells are fully proliferating and initially desynchronized.

Although they are not as directly observable as the previous macroscopic quantities, we can also introduce the instantaneous number of cells undergoing apoptosis at a given time

$$r_f(t) = \iint_{\Omega} \Lambda(x, y, U(t)) \phi_f(t, x, y) dx dy,$$

as well as the cumulative number of apoptotic cells all along the follicular trajectory

$$R_f(t) = \int_0^t r_f(s) ds. \quad (18)$$

Numerical estimation

Given some parameters values, numerical approximations of the outputs (15-18) are computed by solving the model with a finite-volume scheme, implemented on either a uniform or an adaptive mesh as described respectively in [4] and [5]. For a uniform grid where the meshes are defined by

$$\Omega_{i,j} = [i\Delta x, (i+1)\Delta x] \times [j\Delta x, (j+1)\Delta x],$$

the cell density is numerically approximated by

$$\phi_{i,j}^n \approx \int_{\Omega_{i,j}} \phi(t_n, x, y) dx dy.$$

The assessment of MI, original in this paper, requires to identify the meshes of the computation domain whose intersection with $\Omega_{mit} = \{(x, y), p - T_m \leq x < p, \text{ for } p = 1, \dots, N_c, 0 \leq y < y_s\}$ is non void (see right panel Figure 1). It can happen that such meshes overlap only partially with Ω_{mit} . In such a case, the contribution of a mesh to the numerator of the index is proportional to the mesh area included within Ω_{mit} , and we can compute an approximation MI^n of MI at any time step t_n as :

$$MI^n := \frac{\sum_{\Omega_{i,j} \cap \Omega_{mit} \neq \emptyset} |\Omega_{i,j} \cap \Omega_{mit}| \phi_{i,j}^n}{\sum_{\Omega_{i,j} \subset \Omega \setminus \Omega_3} |\Omega_{i,j}| \phi_{i,j}^n},$$

We expose in Appendix A.3 a detailed simulation illustrating the impact of cell cycle exit and apoptosis on the model outputs on different scales and exhibiting the long time behavior of the solution theoretically studied in [19].

3 Characteristic times of the cell dynamics

In this section, we address the problem of computing critical times corresponding to the sequential reaching of the different zones that structure the domain vertically. For the sake of convenience, we will design by ‘‘P+A’’, the zone where apoptosis is superimposed with proliferation, and ‘‘D+A’’ that where it is superimposed with differentiation.

We are specifically interested in the time of entry into (T_{P+A}) or exit from (T_{D+A}), or the exit time (T_e) from the proliferative part of the domain. These times can be roughly associated with crucial steps in follicular development, respectively: the transition from a FSH-responsive to a FSH-dependent state, the transition towards dominance (follicle selected for ovulation), and the exhaustion of the proliferative resources of the follicle at the time of the latest cell cycle exits.

To make possible the direct computation of the cell travel times, we bypass the closed-loop definition of $U(t)$ in (8), to impose instead a simple open-loop time pattern to $U(t)$. We consider the following piecewise-constant definition of the global control $U(t)$

$$U(t) = U^{ol} := \begin{cases} U_{\max}, & \text{for } t \leq T_{s2} \\ U_{\min}, & \text{for } > T_{s2} \end{cases} . \quad (19)$$

The time-evolution of the local control $u_f^{ol}(t)$ is defined within the U_{\min} and U_{\max} bounds of $U(t)$ as

$$u_f^{ol}(t) = \begin{cases} b_1 U_{\max}, & \text{for } t \leq T_{s1} \\ \beta_2 U_{\max}, & \text{for } T_{s1} < t \leq T_{s2} , \\ U_{\min}, & \text{for } t > T_{s2} \end{cases} , \quad (20)$$

where b_1 is the same parameter as in the b_f function, β_2 controls the height of the second plateau, and T_{s1} and T_{s2} are switching times whose definition will be precised in paragraph 3.3, and $b_1 < \beta_2$. This amounts to an open-loop caricature of the pattern followed by $u_f(t)$ in the closed-loop situation, as illustrated in left panel of Figure 2.

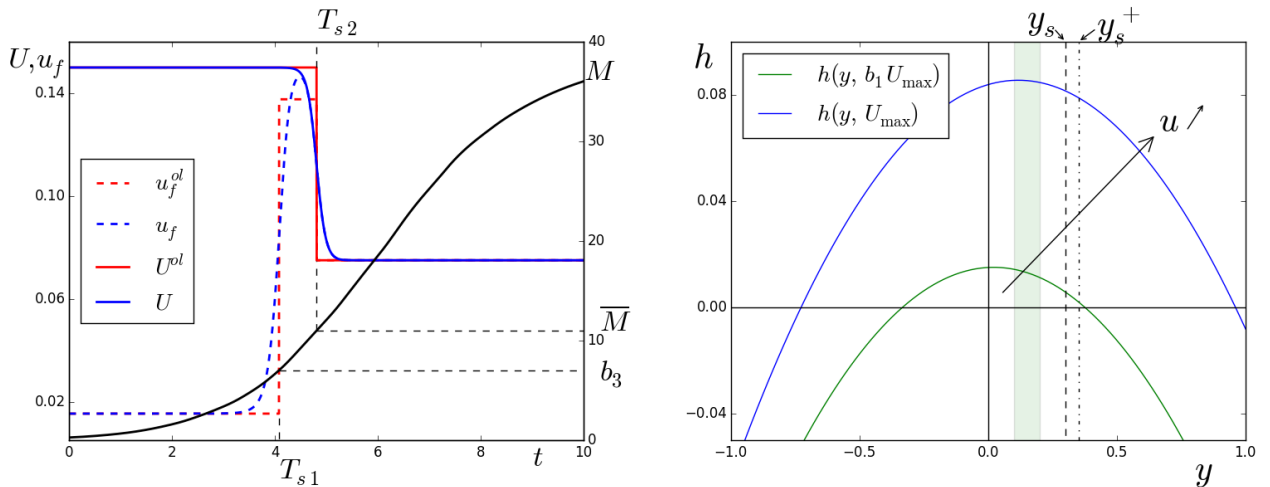


Figure 2: *Left panel: piecewise constant caricature of the $u_f(t)$ input, characterized by 3 different plateaus (sequentially $b_1 U_{\max}$, $\beta_2 U_{\max}$ and U_{\min}). Between the 2 switching times T_{s1} and T_{s2} , the area under the curve is similar in the closed-loop original setup (dashed and solid blue lines) and the caricature (dashed and solid red lines). Right panel: behavior of the maturation function $h(y, u)$ for extremal control values as a function of maturity y for parameter values $c_1 = 0.3$, $c_2 = 0.9$, $\bar{u} = 0.1$, $\tau_h = 0.12$, $b_1 = 0.2$, $U_{\max} = 0.15$. The green shaded area indicates the extremal positions of initial condition $\mu_1 = 0.1$, $\mu_2 = 0.2$.*

Since the cell density is spread out over a range of maturity values at initial time, we assume in this paragraph that the maturation velocity remains positive over the whole

range of y for the control values that we consider (it is indeed possible to find parameters ensuring these properties, as shown in the right panel of Figure 2). Hence the entry (resp. exit) times can be ordered as first entry (resp. exit) time for the cells having the highest initial maturity (μ_2) and last entry (resp. exit) time for the cells having the lowest initial maturity (μ_1). Note that, due to the spreading of initial age over the whole first cycle, the characteristic times computed from a same initial maturity can be different from one initial age to another.

To derive the expression of a chosen characteristic time, we will solve one or both of the following elementary problems, enunciated for constant control values, depending on whether the value of u_f remains constant all over the trajectory or if we have to take into account a switch in the value of u_f .

1. **Free time elementary problem \mathcal{E}_1 :**

Starting from the initial age and maturity (x_0, y_0) and given a target maturity y_1 , compute the time $T(y_1)$ needed to reach y_1 , with associated age $x_1(T)$

$$(x_1, T) = \mathcal{E}_1(y_1; x_0, y_0, u), \quad y_0 < y_1. \quad (21)$$

2. **Fixed time elementary problem \mathcal{E}_2 :**

Starting from the initial age and maturity (x_0, y_0) and given a fixed time interval T , compute the maturity $y_1(T)$ and corresponding age $x_1(T)$ reached after T

$$(x_1, y_1) = \mathcal{E}_2(T; x_0, y_0, u). \quad (22)$$

3.1 Solving the free time elementary problem

We assume that the aging velocity g_f in phase $G1$ or D , is constant between y_0 and y_1 . We consider two cases

Case 1 If $y_0 < y_1 \leq y_s$, $g_f = \gamma_1 u + \gamma_2$, where u is the constant control u_f (we drop the f for the sake of notation saving).

Case 2 If $y_s \leq y_0 < y_1$, $g_f = 1$.

The case $y_0 < y_s < y_1$ can be handled by combining Case 1 to compute the time needed to reach y_s (and corresponding x_s), starting from (x_0, y_0) , with Case 2 to compute the time needed to reach y_1 (and corresponding x_1), starting from (x_s, y_s) .

In both cases, using the factor expression for the maturity velocity h_f

$$h_f(y, u) = -\tau_h(y - r_1(u))(y - r_2(u))$$

where $r_1(u) \leq r_2(u)$ are the roots of the maturation velocity $h_f(y, u)$, we can compute the time spent in $G1$ or D , needed to increase the maturity from y_0 to y_1 as

$$T_{h_f}(y_0, y_1) = \int_{y_0}^{y_1} \frac{dy}{h_f(y, u)} = \frac{1}{\tau_h(r_2(u) - r_1(u))} \ln \left(\frac{y_1 - r_1(u)}{y_1 - r_2(u)} \frac{y_0 - r_2(u)}{y_0 - r_1(u)} \right). \quad (23)$$

In Case 2, T_{h_f} is directly the solution of the elementary problem, with $x_1(T_{h_f}) = x_0 + T_{h_f}$.

In Case 1, things are a little bit more tricky, since the increase in maturity only occurs during phase G1, so that T_{h_f} corresponds only to the time spent in successive G1 phases (T_{G1}), while the solution time T has also to account for the time spent in phase SM, where maturity remains constant (so that the target maturity y_1 is necessarily reached during phase G1).

Hence, $T_{G1} = T_{h_f}$ and $T = T_{SM} + T_{G1}$.

Given that the length of phase G1 is 0.5 and its duration is $t_{G1} = 0.5/g_f$, the number of successive G1 phases covered in T_{G1} is the integer part $\lfloor T_{G1}/t_{G1} \rfloor$. Each G1 phase is separated from the previous one by a SM phase lasting $t_{SM} = 0.5$. The total time T depends on the initial age x_0 , or more precisely the age modulo the length of the cell cycle ($D_c = 1$), $\alpha_0 = x_0 - \lfloor x_0 \rfloor$ (see left panel of Figure 3).

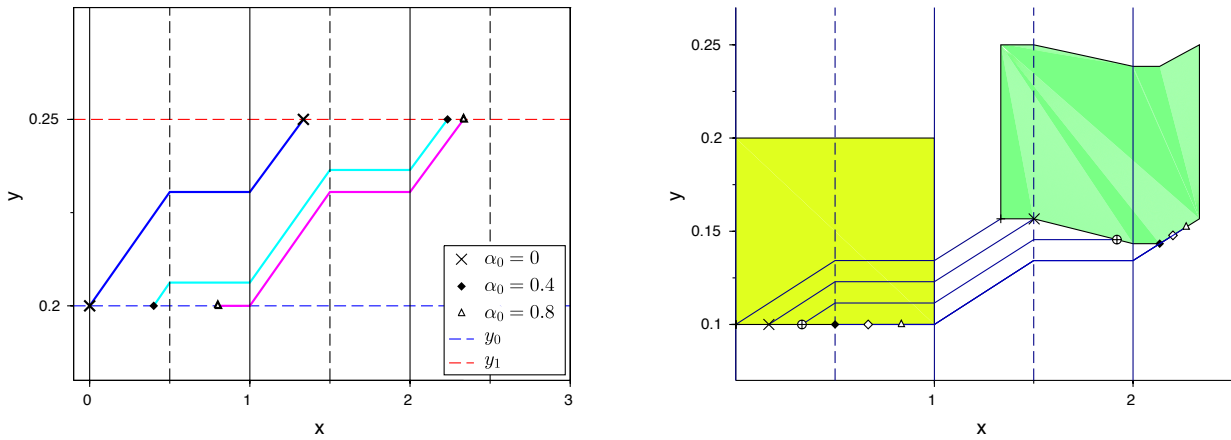


Figure 3: *Left panel: notations and setup for the free time elementary problem with $y_0 = 0.2$ and $y_1 = 0.25$, $\gamma_1 = 1.48$, $\gamma_2 = 0.38$, and other parameter values defined as in Figure 2. The blue path corresponds to a cell starting from phase G1, with $x_0 = \alpha_0 = 0$, that reaches y_1 after $T = 2.58$ at age $x_1 = 1.33$. The cyan path corresponds to a cell starting from phase G1, with $x_0 = \alpha_0 = 0.4$, that reaches y_1 after $T = 3.08$ at age $x_1 = 2.23$. The pink path corresponds to a cell starting from phase SM, with $x_0 = \alpha_0 = 0.8$, that reaches y_1 after $T = 2.78$ at age $x_1 = 2.33$. Right panel: density clouds at time 0 (in yellow) and at time $T = 2.58$ (in green). Solid lines represent paths followed from different initial ages x_0 and same maturity $y_0 = \mu_1 = 0.1$, during the fixed time T . The initial and final positions of a given path are materialized with the same symbol. One can see that, if the cells starting from phase SM follow identical trajectories, they stop at different maturities y according to their initial age x .*

- if $\alpha_0 < 0.5$ the cell starts from phase G1. It takes it $t_{ini} = (0.5 - \alpha_0)/g_f$ to complete the remaining part of phase G1, then 0.5 to cover the SM phase of the first cycle. Then the remaining time $(T_{G1} - t_{ini})$ in phase G1 corresponds to $\lfloor 2(T_{G1} - t_{ini})g_f \rfloor$ complete G1 phases and as many complete SM phases, plus a remaining uncomplete G1 phase

$$\begin{aligned} T(x_0, y_0, y_1) &= T_{G1} + 0.5(1 + \lfloor 2(T_{G1} - t_{ini})g_f \rfloor) \\ &= T_{G1} + 0.5(1 + \lfloor 2T_{G1}g_f - 1 + 2\alpha_0 \rfloor) \end{aligned} \quad (24)$$

The corresponding age is

$$x_1 = T_{G1}g_f + 0.5(1 + \lfloor 2T_{G1}g_f - 1 + 2\alpha_0 \rfloor) + x_0 \quad (25)$$

- if $0.5 \leq \alpha_0 < 1$ the cell starts from phase *SM*. It takes it first $1 - \alpha_0$ to reach the beginning of the next cycle. Then it covers the T_{G1} in *G1* which corresponds to $\lfloor \frac{T_{G1}}{t_{G1}} \rfloor = \lfloor 2T_{G1}g_f \rfloor$ complete *G1* phases and as many complete *SM* phases

$$T(x_0, y_0, y_1) = T_{G1} + 1 - \alpha_0 + 0.5\lfloor 2T_{G1}g_f \rfloor \quad (26)$$

The corresponding age is

$$x_1 = T_{G1}g_f + 1 - \alpha_0 + 0.5\lfloor 2T_{G1}g_f \rfloor + x_0 \quad (27)$$

3.2 Solving the fixed time elementary problem

In the case where $y_1 < y_s$ (as illustrated on right panel of Figure 3), the time T can be broken down as before into the sum of the times spent in several *G1* and *SM* phases

$$T = T_{G1} + T_{SM} = D_{G1}/g_f + D_{SM}. \quad (28)$$

The distance D_{G1} (resp. D_{SM}) covered all along *G1* (resp. *SM*) depends on the starting position in the cycle

$$\text{if } 0 \leq \alpha_0 < 0.5, \quad D_{G1} = k/2 - \alpha_0 + \min(\alpha_1, 0.5), D_{SM} = k/2 + (\alpha_1 - 0.5)^+, \quad (29)$$

$$\text{if } 0.5 \leq \alpha_0 < 1, \quad D_{G1} = (k-1)/2 + \min(\alpha_1, 0.5), D_{SM} = (k+1)/2 - \alpha_0 + (\alpha_1 - 0.5)^+, \quad (30)$$

where $\alpha_1 = x_1 - \lfloor x_1 \rfloor$, $k = (\lfloor x_1 \rfloor - \lfloor x_0 \rfloor) \in \mathbb{N}$, and x_1 is the unknown.

There is a 4 case combinatorial choice for the (α_0, α_1) pair, depending on whether the starting and arrival position lie in phase *G1* or *SM*. After some algebra, we end up with

1. if $0 \leq \alpha_0 < 0.5$

$$k = \lfloor x \rfloor, \text{ with } x = \frac{2(Tg_f + \alpha_0)}{1 + g_f}$$

$$\alpha_1 = \begin{cases} \frac{(1 + g_f)(x - k)}{2} & \text{if } k \leq x < k + \frac{1}{1 + g_f} \\ \frac{(1 + g_f)(x - k) + g_f - 1}{2g_f} & \text{if } k + \frac{1}{1 + g_f} \leq x < k + 1. \end{cases} \quad (31)$$

2. if $0.5 \leq \alpha_0 < 1$

$$k = \lfloor x \rfloor, \text{ with } x = \frac{2g_f(T + \alpha_0 - 1) + 1 - g_f}{1 + g_f}$$

$$\alpha_1 = \begin{cases} \frac{(1 + g_f)(x - k)}{2} & \text{if } k \leq x \leq k + \frac{1}{1 + g_f} \\ \frac{(1 + g_f)(x - k) + g_f - 1}{2g_f} + 1 & \text{if } k + \frac{1}{1 + g_f} \leq x < k + 1. \end{cases} \quad (32)$$

From k and α_1 , we derive $x_1 = \lfloor x_0 \rfloor + k + \alpha_1$, compute D_{G1} using (29) or (30), and then $T_{G1} = D_{G1}/g_f$. Inverting the integral equation (23) where $T_{h_f} = T_{G1}$, we obtain y_1 as

$$y_1(T_{G1}, y_0) = \frac{r_1 - r_2 R}{1 - R}, \quad \text{with } R = \exp(T_{G1} \tau_h (r_2 - r_1)) \frac{y_0 - r_1}{y_0 - r_2}. \quad (33)$$

If y_1 computed from (33) is such that $y_1 \leq y_s$, we are done (see an illustration on Figure 3).

If $y_1 > y_s$, we have to proceed in 2 steps. First we compute from the free time elementary problem the time T_e taken to reach y_s and the corresponding age $x_s(T_e)$. Then we solve the fixed time elementary problem with fixed time $T - T_e$ and starting point (x_s, y_s) , by substituting $T - T_e$ instead of T_{G1} in (33), to obtain finally

$$y_1 = \frac{r_1 - r_2 R}{1 - R}, \quad \text{with } R = \exp((T - T_e) \tau_h (r_2 - r_1)) \frac{y_s - r_1}{y_s - r_2}, \quad x_1 = x_s + T \quad (34)$$

The case $y_0 \geq y_s$ is treated similarly by using (33) with T instead of T_{G1} .

3.3 Combining the two elementary problems to compute the characteristic times

- The first switching time T_{s1} is defined as the minimum time taken by cells starting from the average maturity $(\mu_1 + \mu_2)/2$ to reach the lowest boundary y_s^- of the apoptosis zone

$$T_{s1} = \min_x \{T_1, (x_1, T_1) = \mathcal{E}_1(y_s^-; x, \frac{\mu_1 + \mu_2}{2}, b_1 U_{\max})\}$$

- The second switching time T_{s2} corresponds to the drop in FSH. The exit time is computed as the maximum time taken by cells starting from the lowest maturity μ_1 to reach the differentiation threshold y_s . Since T_{s1} and possibly T_{s2} occur before T_e we have to take into account the changes in the control value

If $T_{s2} \leq T_s$,

$$T_e = T_{s2} + \max_x \{\tau_3, (x_3, \tau_3) = \mathcal{E}_1(y_s; x_2, y_2, U_{\min}),$$

$$(x_2, y_2) = \mathcal{E}_2(T_{s2} - T_{s1}; x_1, y_1, \beta_2 U_{\max}), (x_1, y_1) = \mathcal{E}_2(T_{s1}; x, \mu_1, b_1 U_{\max})\}$$

otherwise,

$$T_e = T_{s1} + \max_x \{\tau_2, (x_2, \tau_2) = \mathcal{E}_1(y_s; x_1, y_1, \beta_2 U_{\max}), (x_1, y_1) = \mathcal{E}_2(T_{s1}; x, \mu_1, b_1 U_{\max})\}$$

Remark: This particle-like approach only deals with time and the cell position within the spatial domain, but it skips out the cell number, since particles are not endowed with any weight linked to the local cell number. Yet, a rough approximation of the time evolution of the global cell number can be derived from assessing the number of complete cell cycles performed by a single particle starting from an average (and median, since the distribution in maturity is uniform) initial maturity $(\mu_1 + \mu_2)/2$:

$$m_f^0(t) = M_0 2^{\lfloor \frac{a(t)}{D_c} \rfloor} = M_0 2^{\lfloor a(t) \rfloor}, \quad \text{for } t \leq T_e. \quad (35)$$

4 Calibration of a single ovulatory trajectory

To perform numerical simulations of the model, we have to instance the numerical values of the parameters listed in Table 1, that either delimit the shape and size of the computation domain, enter the formulation of the mathematical functions involved in the dynamics, or define the initial conditions. In this section, we will detail how we can either fix nominal values for some of the parameters or impose constraints on the bounds of parameter ranges. In the setting of physiologically-oriented multiscale models such as ours, precise functional knowledge is available on the lower scales while quantitative experimental data are rather available on the higher scales. Hence, the question of parameter fitting mainly amounts to inferring the parameters entering the microscopic functions from macroscopic observable variables only. In addition, even on the macroscopic level, data remain rather scarce and are rarely obtained directly as a function of time (but more often as relationships between different variables). Altogether, these difficulties preclude the exclusive use of standard optimization methods to obtain the parameter values. We have thus worked out a calibration strategy combining a priori information on the parameters, deduced from biological knowledge or mathematical properties of the model functions, a posteriori diagnostic on some model outputs, and optimization of the fitting with respect to a training dataset.

Global parameters			Local parameters		
Model	Name	Value	Model	Name	Value
Domain geometry Fig. 1	y_s	0.5	Initial condition	M_0	$[M_{0\min}, M_{0\max}]$
	y_{\max}	1	eq. (41),(51)	μ_1	0.05
	x_s	0.5		μ_2	0.4
	D_c	1	Aging velocity eq. (3)	γ_1	$[0, \gamma_{1\max}]$
Global control eq. (8)	U_{\max}	0.15		γ_2	$[\gamma_{2\min}, g_{\max}]$
	U_{\min}	0.075	Maturation velocity eq. (4)	c_1	$[0, c_{1\max}]$
	c	$[c_{\min}, c_{\max}]$		c_2	$[c_{2\min}, c_{2\max}]$
	\bar{M}	$[M_{\min}, M_{\max}]$		\bar{u}	$[\bar{u}_{\min}, \bar{u}_{\max}]$
δ	1	Mesosopic control eq. (9)	τ_h	$[\tau_{h\min}, \tau_{h\max}]$	
Apoptosis source term eq. (6)	Λ	$[\Lambda_{\min}, \Lambda_{\max}]$		b_1	$[b_{1\min}, b_{1\max}]$
	\bar{y}	$[\bar{y}_{\min}, \bar{y}_{\max}]$		b_2	$[b_{2\min}, b_{2\max}]$
	y_s^-	0.45		b_3	$[b_{3\min}, b_{3\max}]$
	y_s^+	0.55			

Table 1: *List of parameters. Global parameters, common to all follicles in the cohort and local parameters, specific to individual follicles. Some parameters are given nominal values in all cases, while others are constrained to bounding conditions but may vary from one simulation or one follicle to another.*

All our numerical simulations will be illustrated in the ewe. Indeed, large domestic species, and especially the ovine species, are particularly interesting to investigate the bases of follicular development, since (i) they have a large body size allowing repeated blood sampling and further analysis of endocrine time series, (ii) the duration of the ovarian cycle makes it easier to dissect the different steps in the temporal sequence of hormonal feedbacks between the ovaries and hypothalamo-pituitary axis and its links with the follicle selection process, (iii) they are closer to human ovarian physiology compared to rodents, and (iv) there exist in several ewe strains natural mutations affecting the ovulation number, that correspond to different genetic strategies of poly-ovulation [26]. Many experimental studies have been undertaken on follicular development in this species, so that we can access a variety of experimental data ranging from cell kinetics of granulosa

cells or in vivo monitoring of follicle growth to endocrine time series of pituitary and ovarian hormones.

4.1 Domain geometry: $x_s, D_c, y_s, y_s^-, y_s^+, y_{\max}$

The dynamics of a follicle's trajectory is mostly characterized by the transit times within the different phases of the computation domain. As explained in the previous section, the transit time from the initial to the maturity threshold y_s controls the instant of cell cycle exit, hence the maximum cell count; similarly, the transit time within the apoptotic zone controls the cumulative exposure to apoptosis, hence the cumulative cell loss.

For rather obvious computation purposes, the freedom degrees that we use to control the transit times both horizontally and vertically are the aging and maturation velocities, while the length and height of the domain subparts are kept constant and can be set to any arbitrary value. Hence, the geometry of the computation domain is fixed once for all, with the additional constraints that the domain subparts are paved by an integer number of meshes and that the same discretization step is used in both direction $\Delta x = \Delta y$. Choosing as unit length the duration of the cell cycle, D_c , we thus have $y_{\max} = 1$, and, for the sake of simplicity, we set $x_s = y_s = 1/2$ (this amounts to multiplying the time by a scaling factor (here 2/3) to recover the physical time scale in days, for an average cell cycle duration of one day).

Also, the boundaries of the apoptotic zone, y_s^- and y_s^+ should coincide with horizontal boundaries between two consecutive meshes. From the hypotheses underlying the choice of $\Lambda(y, U)$, we can consider that the support of this function is rather narrow, and represents one tenth of the height of phase G1 and D on either side of the $y = y_s$ boundary. Setting the values of y_s^- and y_s^+ imposes the value of \bar{y} .

4.2 Specification-based constraints on the parameters

From the bibliographic corpus dedicated to terminal follicular development in the ewe, we can draw-up a list of specifications that should be fulfilled either by the parameters or some model outputs. Part of these specifications are summarized in a dataset first introduced in [7], that relates the cell number to the follicular age (red bullets on Figure 4), by combining data on follicular growth (changes in diameter assessed either by histology [34] or ultrasonography [24]) with data on granulosa cell numbers according to the diameter [32]. The initial age corresponds to 1mm in diameter follicles, when ovarian follicles undergo at this size their maximal proliferative activity ([33, 34]) and can be recruited into the selection process [31]. This set of data will be used as such, in the optimization part of the calibration strategy (see next sections) or as a guide to define the checklist that any ovulatory trajectory should fulfill. From this dataset, we can derive constraints on the range of cell values that should be reached at some critical points of follicular development, that are given in the literature with respect to the diameter, and that we can convert in time:

1. the switch from a FSH-responsive to a FSH-dependent status in follicles 2.5mm in diameter [26, 20]; from this diameter, the follicles become unable to pursue their development further if they are not supplied with FSH (as it has been shown in many occasions of surgical or pharmacological hypophysectomy);

2. the selection of the future ovulatory follicles around 4mm in diameter ; at this diameter, the drop in the growth fraction is the highest [23], as is the sensitivity towards FSH, as assessed by the rate of follicle degeneration [26]; dominant follicles are “saved” thanks to their new ability to transfer their gonadotropin dependency from FSH to LH (luteinizing hormone);
3. the ovulation at an ovulatory size around 7-7.5mm in the mono-ovulatory strains of sheep ; at this size, one can assess the ratio of increase CC in the cell number from the initial cell number at diameter 1mm:
 $CC \in [CC_{\min}, CC_{\max}] \approx [25, 35]$; since in the ovulatory case the cell number starts stabilizing as soon as the maturity of all cells overcomes y_s^+ , this ratio also gives a rough indication on the bounds of the global maturity of the ovarian follicle from selection to ovulation: $m_f^1(t) \in [CC_{\min}y_s^+, CC_{\max}y_{\max}]$.

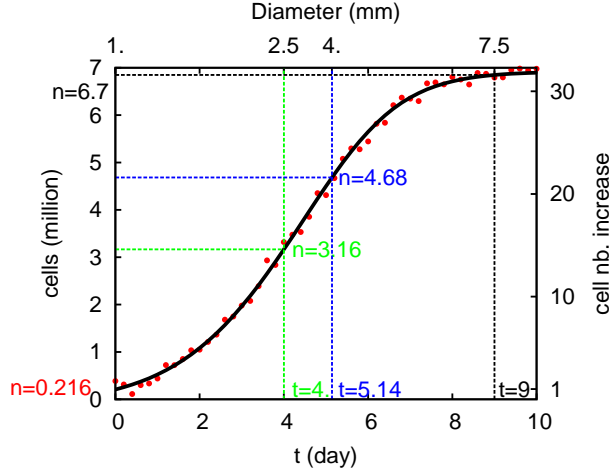


Figure 4: Specifications on the cell number in an ovulatory follicle. The cell number is shown both as a function of diameter (top horizontal axis) and time (bottom horizontal axis). From the initial cell number (≈ 0.216), 3 checkpoints can be defined from the biological knowledge and applied to our training data set (red bullets superimposed on the solid black line) ; we expect to reach given cell numbers at the time when the follicle switches from a FSH-responsive to a FSH-dependent status (green marks, diameter 2.5mm), when it switches from a mainly proliferative ($GF > 0.5$) to a mainly differentiated status (blue marks, diameter 4mm) and when it reaches the ovulatory size (diameter 7.5mm, where the cell number gets stabilized). The cell number is illustrated in physical unit (million of cells) on the left vertical axis, and as the ratio of increase from the normalized initial number on the right vertical axis.

Besides these specifications, the bounds of the $S(M(t))$ function given in equation (7) can be set in a more straightforward way, since they can be read from time series of FSH plasma levels along the ovarian cycle (see e.g. [24, 30]). During the time horizon spanned by the model, the FSH level starts from its maximum and drops by half at the end of the follicular phase. Hence we can set $U_{\min} = U_{\max}/2$. We can also get some a priori idea on the location of the inflexion point ruled by the value of \bar{M} and consider that

$$CC_{\min}y_s^+ \leq \bar{M}_{\min} \leq \bar{M} \leq \bar{M}_{\max} \leq CC_{\max}y_{\max}$$

which amounts to assume that the dominant follicle contributes the most to the FSH drop.

We can also readily define the initial conditions. First, we consider that the distribution in age covers the whole first cell cycle and that it takes into account the discontinuities in the aging velocity on the internal boundaries as defined by equation (42). For the distribution in maturity, the upper bound is defined from the expected time taken by a cell with initial maturity μ_2 to reach the apoptotic zone (start of FSH-dependency), while the lower bound is defined from the expected time taken by a cell with initial maturity μ_1 to exit the cell cycle (time of stabilization in the cell number). Finally, the total cell number is fixed from the pseudo-data set to $\approx 2 \cdot 10^5$ cells.

Finally, we can propose bounds for the parameters $\gamma_1, \gamma_2, c_1, c_2$ in the velocity functions. The derivation of these bounds is detailed in Appendix B, we just comment here the underlying principles. First, the velocities are functions of the control term $u_f(t)$, whose values cover a closed interval determined by the bounds of $U(t)$ and the parameter of the (closed loop or piecewise constant version of) b_f function, so that we can restrict the study to the admissible values of $u_f(t)$. Second, there are specific assumptions on the roots of h_f needed to ensure that the velocity is positive in the proliferative part of the domain ($r_2(u, \gamma) > \gamma_s$ for all admissible u) and to discriminate the ovulatory trajectories from the atretic ones in a FSH-poor environment (see [15]). Lastly, the modulation operated by the control term on the aging velocity in phase G_1 is moderate and is fixed by a modulation coefficient of $r\%$ (set to 10% in practice).

4.3 Characteristic time based calibration of an ovulatory trajectory

Even if we have fixed bounds for several parameters, the dimension of the parameter space remains large with 14 unknown parameter values. As a consequence the direct optimization-based estimation of these parameters is very costly, as each trial requires a 2D Finite Volume simulation. To circumvent this problem, we design a multi-step method that combines:

- The identification of the parameters entering functions $u_f^{ol}, U^{ol}, h_f, g_f$ from a multi-objective criterion based on the characteristic times. This step (Step 1 in Figure 15) performs the identification of 9 parameter values with little a priori information, which is compensated by the low computing time cost of the particle-like model.
- The fitting of the parameters entering functions $u_f, U, h_f, g_f, \Lambda$ to the pseudo data set. This step (Step 3 in Figure 15) starts from an appropriate initial guess for most of the 8 parameters so that the 2D FV-based identification remains tractable.

Appendix C.1 details the expressions of the multi-objective functions used along the different calibration steps and describes the practical algorithm implemented to seek local minima by means of the CMAES Python library [12]. An instance of an ovulatory trajectory is presented in the top panels of Figure 5. The macroscopic outputs of the models (cell number and follicular maturity) are similar in the open loop (dashed lines) and closed loop (solid lines) situations.

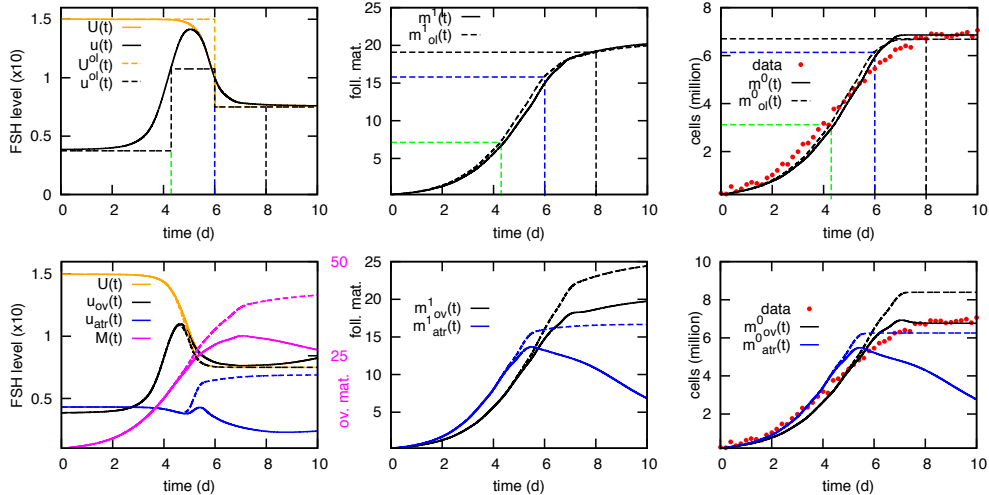


Figure 5: *Single ovulatory follicle (top panels) and pair of atretic and ovulatory follicles (bottom panels). Left panels: control values, center panels: follicular maturities, right panels: cell numbers. In the single follicle case dashed lines correspond to the open loop situation and solid lines to the closed loop one. In the case of the atretic-ovulatory pair dashed lines correspond to the trajectory when the apoptosis rate is deactivated ($\bar{\Lambda} = 0$).*

5 Calibration of interacting ovulatory and atretic trajectories

We finally dispose of a reasonable parameter set p_{ov} (see values in Table 2) for a closed-loop ovulatory trajectory.

We now consider the interaction between several follicles, resulting in a situation with ovulatory follicles and atretic ones.

- Starting with a pair of interacting follicles we first couple the ovulatory trajectory with another trajectory corresponding to an atretic follicle: another multi-objective function, formulated in Appendix C.2, is introduced to ensure that for the atretic follicle, the cell number increases significantly with respect to its initial value, up to the selection time, while the cell loss becomes substantial after this time, with a final cell number clearly lower than the maximal number reached along the atretic trajectory [16].
- We then design a realistic cohort of N_f follicles: for a given number of ovulations N_{ov} , we couple trajectories obtained by N_{ov} (respectively $N_f - N_{ov}$) random fluctuations about the ovulatory (resp. atretic) parameter set and adapt the global parameters in functions $U(t)$ and $\Lambda(t)$.

An instance of an ovulatory/atretic pair is presented in the bottom panels of Figure 5 (solid lines)*. To visualize the contribution of the apoptotic process in the dynamics, the same pair is also followed in the case when the apoptosis rate is deactivated ($\bar{\Lambda} = 0$,

*A movie showing the corresponding changes in the cell density is available as supplementary material.

dashed lines); the selection is then not operated and the former atretic follicle becomes able to ovulate.

Figure 6 displays the macroscopic outputs for a cohort of 10 follicles. The random perturbations are uniformly distributed within $\pm 10\%$ of the parameters in Table 1. The ovulation time T_{ov} is defined as the time when the cumulated ovarian maturity $\int_0^{T_{ov}} M(s)ds$ (magenta dashed line in Figure 6) has reached a level sufficient to trigger ovulation (840 in this simulation). The follicles are sorted amongst ovulatory follicles (black, blue and green solid lines) and atretic ones (dashed lines). After T_{ov} all follicles whose maturity reaches a theshold (here 15) within one day ovulate.

The top panels display a simulation where all 10 follicles start with the same normalized cell number. At ovulation time $T_{ov} = 8$ only follicles 1 to 3 have reached a sufficient maturity to ovulate. Follicle 4 (dashed blue line) is yet just below the threshold. The bottom panels display the situation where follicles 4 and 5 start with an enhanced cell number of 1.25 instead of 1 for the seven other follicles. The ovulation time occurs a bit earlier ($T_{ov} = 7.8$) and by that time both follicles 4 and 5 have managed to reach the ovulatory stage.

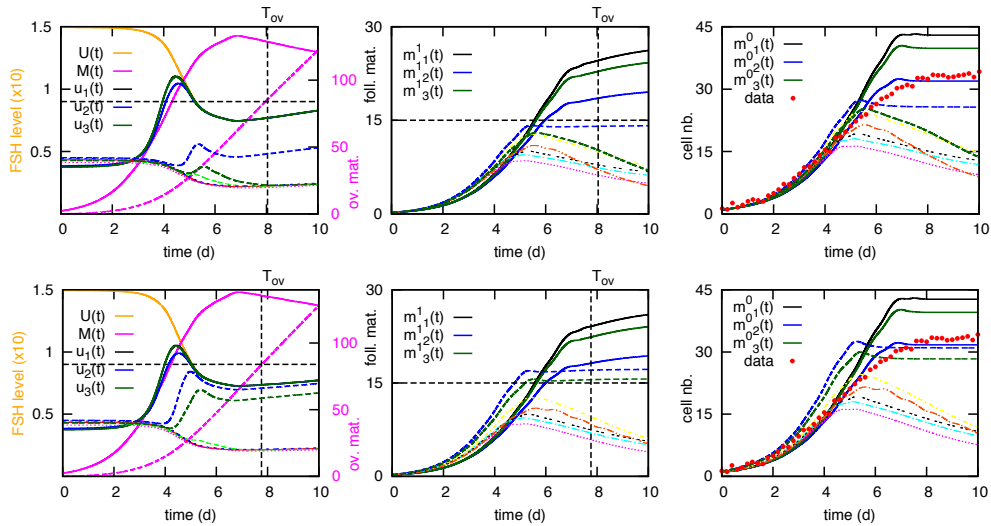


Figure 6: *Cohort of 10 interacting follicles. Left panels: control values, center panels: follicular maturities, right panels: cell numbers. Trajectories of follicles 1, 2, and 3 (respectively 4 to 7) result from random perturbations applied to the ovulatory (resp. atretic) follicle in Figure 5. Compared to top panels, follicles 4 and 5 in bottom panels (dashed green and blue lines) start with a cell number increased by 25%. Dashed black lines indicate the ovulation thresholds. The magenta dashed line is the time integral of $M(t)$ (scaled by 10 for the sake of lisibility).*

6 Discussion

In this work, we have tuned the quantitative behavior of a multiscale model coupling cell kinetics with population dynamics, and spanning scales from the intracellular level (FSH-dependent expression of the velocities, and especially of the maturation function,

whose biochemical foundations were settled in [9]) to the tissue (ovarian follicle) level. The passage from microscopic to macroscopic dynamics is based, for a single follicle, on the numerical computation of moments and derived outputs such as cell kinetics indexes (growth fraction and mitotic index) and the total cell number. In addition, the connections between scales are not limited to an averaging approach, but they are rather two-way, since the macroscopic interactions between follicles, mediated by the pituitary-ovarian loop, feedback onto the microscopic level.

To calibrate the model parameters, we have investigated thoroughly the links between cell kinetics indexes and the fine distribution of cells within the different cell states (proliferating or differentiated) and cell cycle phases ; in some sense, we revisit and extend a corpus of biomathematical works that were undergone at the golden age of experimental and theoretical cell kinetics (in the 1970s, see for instance [2]), that studied the impact of different cell distributions (exponential in case of non-limited growth, uniform in case of strict population renewal, possibly subject to cell loss) on the interpretation of experimental cell-kinetics approaches. We have benefited from both the richness of our 2D-structuring of the cell population (versus only an age-structuring) and the power of numerical simulations to tackle more complex situations including time-dependent and even unknown-dependent progression along the cell cycle (see Section A.3 in Appendix A).

At this stage, the biomathematical approach is somehow a step forward on compared to the experimental possibilities, since it is still very difficult to obtain quantitative information on cell dynamics in physiological conditions. For instance, even “simple” cell counting represents a hard-working process, and most of the time, there are not true kinetic data, since, due to the invasive character of the measurements, different experimental subjects correspond to the different time points (as often in physiological issues, time is thus a statistical reconstruction in this case). Yet, one may hope that cutting edge techniques allowing one to visualize the cell cycle distribution in living cells [25], that requires the transfection of cells, will also be easily deployable in more physiological contexts, or that time-lapse monitoring of cell fate (see e.g. [14, 21]) will be usable on larger time and space scales to embed single cell fates within a tissue dynamics.

From the reproductive biology viewpoint, our results have shown that the hormonal control is at the source of selection, since there is no predestination of follicles, neither on the proliferative capital issue (all follicles can potentially reach a similar total cell number at the end of development) nor on the apoptosis issue (any follicle will escape from the apoptosis zone when exposed to a constantly favorable environment). With minimal follicular heterogeneity in the parameters affecting only the velocities (and possibly as a first trial instance initial conditions), and a quite narrow range of FSH levels, selection can nevertheless be operated through the model. We have already mentioned and investigated in former studies the importance of managing the proliferative resource of the follicles and controlling the transit time in the apoptosis zone, on the level of a single follicle [8]. One critical point that has been further unraveled by the current study, on the level of the population of interacting follicles, is that there is a relatively little room for manoeuvre to meet at the same time the constraints that (i) the ovulatory follicle(s) should not have a too high cumulated loss of cells and (ii) the atretic follicle should in contrast be subject to a significant cell loss.

To perform the parameter tuning, we have had to cope with the structural lack of quan-

titative and kinetic data on in-vivo follicular development. Everything would be much simpler if datasets giving the cell numbers of both ovulatory and atretic follicles against time were available. We thus had to develop a more indirect strategy that brute-force fitting and we could not proceed only through optimization steps. The core of our strategy is the computation of characteristic reaching times in the spatial domain from a particle-like reduction of the model exposed in section 3. Even if it is not a genuine reduced model of the original PDE system, since the particles are not weighted (hence the cell mass is not explicitly computable), the main advantage of this approach is to account rigorously for the impact of phase-dependent velocities on the dynamics and to discriminate precisely the trajectories according to the initial age of cells (i.e. their specific location within the cell cycle). This is a key point that has enabled us to find out a suitable initial guess that can be thereafter refined progressively along a sequence of optimization steps. The drawback of the calibration strategy is that at this stage, we cannot assess our parameter sets from the viewpoint of identifiability; we rather provide a set of compatible parameters. Issues of identifiability and statistical estimation could be studied through intensive simulations with random selection of the parameter values ; the idea would be to recover for each parameter a distribution compatible with all the specifications, which would provide us with information on the heterogeneity and variability in the parameters with respect to different physiological (mono- or poly-ovulation) or pathological (dysovulation or anovulation) situations.

We have performed the numerical illustration and parameter fitting of the model in the ewe due to the variety of datasources available in the ovine species, and also because this species exhibits a natural (and genetically-encoded) variability in the ovulation number, that is challenging both on the experimental side and the modeling one. The principle of our approach could be generalized to other species and especially to the human (mono-ovulating) species. We intend to extend the present model of terminal follicular development to women. From the mathematical viewpoint, this extension would not raise new bottlenecks. Yet, from the biomathematical, data-based viewpoint, it is not straightforward, since it requires to design a specification list, as we did for the ewe, from very composite information that need to be both gathered and tallied from literature articles dealing with morphologic (monitoring of follicle growth through ultrasonography), histologic, cell kinetics and endocrine issues.

References

- [1] M. Adimy, F. Crauste, and S. Ruan. A mathematical study of the hematopoiesis process with applications to chronic myelogenous leukemia. *SIAM J. Appl. Math.*, 65:1328–1352, 2005.
- [2] W.A. Aherne, R.S. Camplejohn, and N.A. Wright. *An introduction to cell population kinetics*. Edward Arnold, 1977.
- [3] B. Aymard, F. Clément, F. Coquel, and M. Postel. Numerical simulation of the selection process of the ovarian follicles. *ESAIM Proc.*, 28:99–117, 2012.

- [4] B. Aymard, F. Clément, F. Coquel, and M. Postel. A numerical method for transport equations with discontinuous flux functions: Application to mathematical modeling of cell dynamics. *SIAM J. Sci. Comput.*, 35:6, 2013.
- [5] B. Aymard, F. Clément, and M. Postel. Adaptive mesh refinement strategy for a non conservative transport problem. *ESAIM Math. Model. Numer. Anal.*, 90:4, 2014.
- [6] F. Clément, J.-M. Coron, and P. Shang. Optimal control of cell mass and maturity in a model of follicular ovulation. *SIAM J. Control Optim.*, 51(2):824–847, 2013.
- [7] F. Clément, M.-A.Gruet, P. Monget, M. Terqui, E. Jolivet, and D. Monniaux. Growth kinetics of the granulosa cell population in ovarian follicles: an approach by mathematical modelling. *Cell Prolif.*, 30:255–570, 1997.
- [8] F. Clément and D. Monniaux. Multiscale modelling of follicular selection. *Prog. Biophys. Mol. Biol.*, 113(3):398–408, 2013.
- [9] F. Clément, D. Monniaux, J. Stark, K. Hardy, J.-C.Thalabard, S. Franks, and D. Claude. Mathematical model of FSH-induced cAMP production in ovarian follicles. *Am. J. Physiol. (Endocrinol. Metab.)*, 281:E35–E53, 2001.
- [10] N. Echenim, F. Clément, and M. Sorine. Multi-scale modeling of follicular ovulation as a reachability problem. *Multiscale Model. Simul.*, 6(3):895–912, 2007.
- [11] N. Echenim, D. Monniaux, M. Sorine, and F. Clément. Multi-scale modeling of the follicle selection process in the ovary. *Math. Biosci.*, 198:57–79, 2005.
- [12] N. Hansen and A. Ostermeier. Adapting arbitrary normal mutation distributions in evolution strategies: The covariance matrix adaptation. In *Evolutionary Computation, 1996., Proceedings of IEEE International Conference on*, pages 312–317. IEEE, 1996.
- [13] N.R. Hartmann and Pedersen T. Analysis of the kinetics of granulosa cell populations in the mouse ovary. *Cell Tissue Kinet.*, 3(1):1–11, 1970.
- [14] W. Haubensak, A. Attardo, W. Denk, and W.B. Huttner. Neurons arise in the basal neuroepithelium of the early mammalian telencephalon: A major site of neurogenesis. *Proc. Natl. Acad. Sci. U.S.A.*, 101(9):3196–3201, 2004.
- [15] J.Y. Jiang, G. Macchiarelli, B.K. Tsang, and E. Sato. Capillary angiogenesis and degeneration in bovine ovarian antral follicles. *Reproduction*, 125:211–223, 2003.
- [16] P.D. Jolly, P.R. Smith, D.A. Heath, N.L. Hudson, S. Lun, L.A. Still, C.H. Watts, and K.P. McNatty. Morphological evidence of apoptosis and the prevalence of apoptotic versus mitotic cells in the membrana granulosa of ovarian follicles during spontaneous and induced atresia in ewes. *Biol. Reprod.*, 56(54):837–846, 1997.
- [17] T. Maekawa and J. Tsuchiya. A method for the direct estimation of the length of G1, S and G2 phase. *Exp. Cell Res.*, 53:55–64, 1968.

- [18] E.A. McGee and A.J. Hsueh. Initial and cyclic recruitment of ovarian follicles. *Endocr. Rev.*, 21(2):200–214, 2000.
- [19] P. Michel. Multiscale modeling of follicular ovulation as a mass and maturity dynamical system. *Multiscale Model. Simul.*, 9:282–313, 2011.
- [20] D. Monniaux, C. Huet, N. Besnard, Clément F., M. Bosc, C. Pisselet, P. Monget, and J.C. Mariana. Follicular growth and ovarian dynamics in mammals. *J. Reprod. Fertil. Suppl.*, 51(1):3–23, 1997.
- [21] S.C. Noctor, V. Martínez-Cerdeño, L. Ivic, and A.R. Kriegstein. Cortical neurons arise in symmetric and asymmetric division zones and migrate through specific phases. *Nature Neurosci.*, 7(2):136–144, 2004.
- [22] B. Perthame. *Transport Equations in Biology*. Birkhäuser Verlag, Basel, 2007.
- [23] C. Pisselet, F. Clément, and D. Monniaux. Fraction of proliferating cells in granulosa during terminal follicular development in high and low prolific sheep breeds. *Reprod. Nutr. Dev.*, 40:295–304, 2000.
- [24] J. P. Ravindra, N. C. Rawlings, A. C. O. Evans, and G. P. Adams. Ultrasonographic study of ovarian follicular dynamics in ewes during the oestrous cycle. *J. Reprod. Fertil.*, 101(2):501–509, 1994.
- [25] A. Sakaue-Sawano, H. Kurokawa, T. Morimura, A. Hanyu, H. Hama, H. Osawa, S. Kashiwagi, K. Fukami, T. Miyata, H. Miyoshi, T. Imamura, M. Ogawa, H. Masai, and A. Miyawaki. Visualizing spatiotemporal dynamics of multicellular cell-cycle progression. *Cell*, 132(3):487 – 498, 2008.
- [26] R.J. Scaramuzzi, D.T. Baird, B.K. Campbell, M.-A. Driancourt, J. Dupont, J.E. Fortune, R.B. Gilchrist, G.B. Martin, K.P. McNatty, A.S. McNeilly, P. Monget, Monniaux D., C. Viñoles, and R. Webb. Regulation of folliculogenesis and the determination of ovulation rate in ruminants. *Reprod. Fertil. Dev.*, 23:444–467, 2011.
- [27] P. Shang. Cauchy problem for multiscale conservation laws: Application to structured cell populations. *J. Math. Anal. Appl.*, 401(2):896–920, 2013.
- [28] P. Shang and Z. Wang. Analysis and control of a scalar conservation law modeling a highly re-entrant manufacturing system. *J. Differential Equations*, 2(250):949–982, 2011.
- [29] CL Smith and PP Dendy. Relation between mitotic index, duration of mitosis, generation time and fraction of dividing cells in a cell population. *Nature*, 193:555, 1962.
- [30] B.M. Toosi, S.V. Seekallu, and N.C. Rawlings. Effects of the rate and duration of physiological increases in serum fsh concentrations on emergence of follicular waves in cyclic ewes. *Biol. Reprod.*, 83(4):648–655, 2010.

- [31] C. G. Tsonis, L. P. Cahill, R. S. Carson, and J. K. Findlay. Identification at the onset of luteolysis of follicles capable of ovulation in the ewe. *J. Reprod. Fertil.*, 70(2):609–614, 1984.
- [32] C.G. Tsonis, R.S. Carson, and J.K. Findlay. Relationships between aromatase activity, follicular fluid oestradiol-17 β and testosterone concentrations, and diameter and atresia of individual ovine follicles. *J. Reprod. Fert.*, 72:153–163, 1984.
- [33] K.E. Turnbull, A.W. Braden, and P.E. Mattner. The pattern of follicular growth and atresia in the ovine ovary. *Aust. J. Biol. Sci.*, 30(3):229–241, 1977.
- [34] K.E. Turnbull, P.E. Mattner, J.M. George, and R.J. Scaramuzzi. The relation between patterns of ovarian follicle growth and ovulation rate in sheep. *Aust. J. Biol. Sci.*, 31(6):649–655, 1978.
- [35] J.J. Tyson and B. Novak. Temporal organization of cell cycle. *Curr. Biol.*, 18:R759–768, 2008.

A Computation of the age distribution within the cell cycle and related cell kinetics indexes in simplified frameworks

A.1 Simple exponential cell dynamics

We derive below the computation of the MI in the simplest case of a desynchronized and fully proliferating cell population, with a constant velocity g of progression along the cell cycle, and without any cell cycle exit process such as differentiation or apoptosis. In the 2D framework described by the master equation (1), we thus remove the source term, set the maturation function to a constant null value, and initialize the density uniformly in maturity over the whole first cell cycle. With these assumptions, the 2D framework, in which the maturity distribution is uniform in space and constant over time, amounts to a 1D framework,

$$\partial_t \psi(x, t) + \partial_x (g\psi(x, t)) = 0, \quad (36)$$

but we can still follow the progression of the cell density on the 2D domain (rather than on a line), which makes the visualization easier. In this simple framework, we can easily illustrate the computation of the MI. Starting from an exponential initial condition $\psi_0(x) = Ce^{-kx}$, C and k are chosen such that $\psi_0(0^+) = \psi_0(D_c^-)$ and $\int_0^{D_c} \psi_0(x) dx = 1$, which leads to $k = \frac{\ln 2}{D_c}$ and $C = \frac{2 \ln 2}{D_c}$.

The simplified transport equation (36) with periodically-doubling boundary conditions $\psi(t, 0^+) = 2\psi(t, D_c^-)$ provides the solution for the density at all time

$$\psi(t, x) = Ce^{-\ln 2 \frac{gt}{D_c} e^{-kx}} = 2^{\frac{gt}{D_c}} \psi_0(x), \quad (37)$$

which highlights the stationary nature of the age distribution. From this formula, we can recover the macroscopic outputs, defined earlier, which come into play in the definition of the MI. The total cell number at time t is

$$N(t) = \int_0^{D_c} \psi(t, x) dx = \int_0^{D_c} 2^{\frac{gt}{D_c}} \psi_0(x) dx = 2^{\frac{gt}{D_c}} \frac{C}{k} (e^{-kD_c} - 1) = 2^{\frac{gt}{D_c}}$$

The number of cells within Ω_{mit} at time t is

$$N_{mit}(t) = \int_{D_c - T_m}^{D_c} \psi(t, x) dx = 2^{\frac{gt}{D_c}} (e^{kT_m} - 1)$$

Therefore, for all t , $0 \leq gt \leq 1$ the mitotic index (17) is constant and equal to

$$MI(t) = e^{kT_m} - 1 = e^{\frac{\ln 2}{D_c} T_m} - 1, \quad (38)$$

which is a classical formula (see e.g. [29]). The x, y functional domain can also be used to illustrate the progression from one cell cycle to the subsequent one ; instead of a periodic domain in x we unfold the subsequent cell cycles in order to keep track of the cell generation.

Redefining the initial condition as

$$\psi_0(x) = \begin{cases} Ce^{-kx} & \text{for } 0 \leq x \leq D_c \\ 0 & \text{for } D_c < x \end{cases},$$

the solution is transported with velocity g and doubled when it crosses the mitosis interface $x = nD_c$, $n = 1, 2, \dots$. A simple recursion leads to the general solution, for $t \geq 0$, $x \geq 0$

$$\psi(t, x) = \begin{cases} 2^n Ce^{-k(x-gt)} & \text{for } nD_c \leq x \leq (n+1)D_c \text{ and } (x-D_c)/g \leq t \leq x/g \\ 0 & \text{elsewhere} \end{cases}. \quad (39)$$

Figure 7 shows some snapshots of both the $\phi(t, x, y)$ density (color-code based panels) and the $\psi(t, x)$ density (graphs with red curves), in the simplified 2D framework. In the case of a single cell cycle with periodic boundary conditions (top panels in Figure 7), the age distribution is the exponentially decreasing in age and increasing in time law (37). In the case of two (or more) successive cycles (bottom panels in Figure 7), the shape of the density is modified at the time of the transition between the consecutive cycles, since the cells are in between the two cycles, and then goes back to the simple exponential pattern once all cells have exited the first cell cycle and lie in the second one. Figure 8 displays the corresponding macroscopic outputs in the total cell number $m_f^0(t)$ (eq. 15) and mitotic index $MI(t)$. As expected, the cell number is doubled after one cell cycle, while the numerical MI (19) remains constant and equal to the theoretical value expected from (38).

A.2 Phase dependent cell dynamics: impact on the progression of cells along the cell cycle

We now consider the case of a cell cycle with different, yet constant velocities according to the cell phases: $g \neq 1$ in $G1$ phase and $g = 1$ in SM phase. To take into account the velocity discontinuity on the interface between the $G1$ and SM phase, we introduce a discontinuous initial condition,

$$\psi(0, x) = \psi_0(x) = \begin{cases} M_0 C_{G1} e^{-kx_s} & \text{for } 0 \leq x < x_s \\ M_0 C_{SM} e^{-kx_s} & \text{for } x_s \leq x < D_c \end{cases} \quad (40)$$

We impose conditions of flux continuity at $x = x_s$ and flux doubling on the periodic boundary $x = 0$ and $x = D_c$

$$\begin{aligned} gC_{G1}e^{-kx_s} &= C_{SM}e^{-kx_s} \\ gC_{G1} &= 2C_{SM}e^{-kD_c} \end{aligned}$$

plus a normalization condition

$$\int_0^{D_c} \psi_0(x) dx = M_0 \quad (41)$$

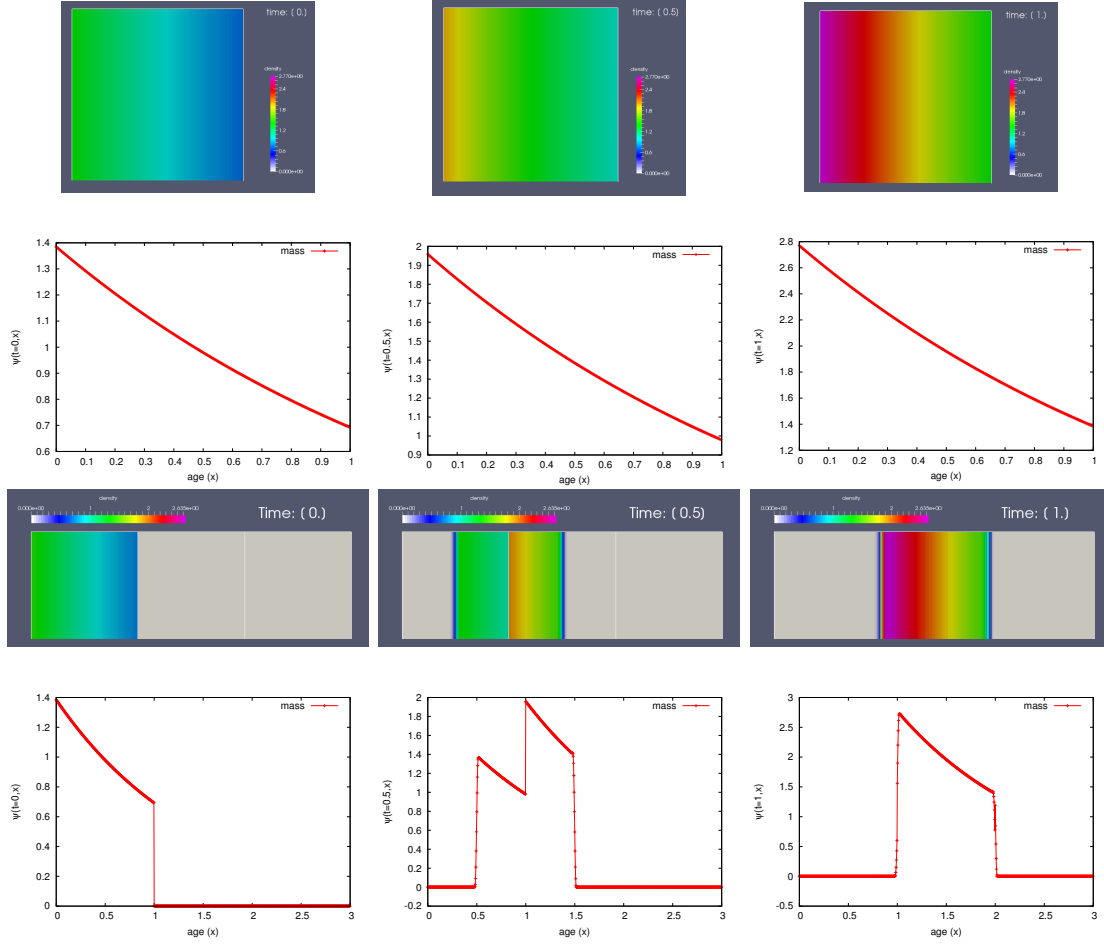


Figure 7: Snapshots of the cell density $\phi(t, x, y)$ over the 2D domain (color-code panels) and age density $\psi(t, x)$ (red curves) in the case of a fully proliferating, desynchronized cell population, with constant velocity ($g = 1$) of progression along the cell cycle. Top panels: a single cell cycle with periodic boundary conditions. Bottom panels: 2 subsequent cell cycles. Left panels: $t = 0.0$, middle panels: $t = 0.5$, right panels $t = 1$.

from which we obtain

$$\begin{aligned}
 k &= \ln(2)/D_c \\
 C_{G1} &= \frac{2 \ln(2)}{D_c(2 + 2^{\frac{1-x_s}{D_c}}(g-1) - g)} \\
 C_{SM} &= gC_{G1}
 \end{aligned}$$

and, replacing in (40),

$$\psi_0(x) = \begin{cases} M_0 C_{G1} 2^{-x/D_c} & \text{for } 0 \leq x < x_s \\ M_0 C_{SM} 2^{-x/D_c} & \text{for } x_s \leq x < D_c \end{cases}. \quad (42)$$

The solution to (36) is no longer explicit but can be derived recursively, as done in [5]: we recall briefly the result here for a series of N_c cycles (hence $2N_c - 1$ interfaces), with $D_c = 2x_s$. On the p th interface located at $x = p \times x_s$ the condition on the flux reads:

$$v_p \psi(t, px_s^+) = k_p v_{(p-1)} \psi(t, (p-1)x_s^-) \quad (43)$$

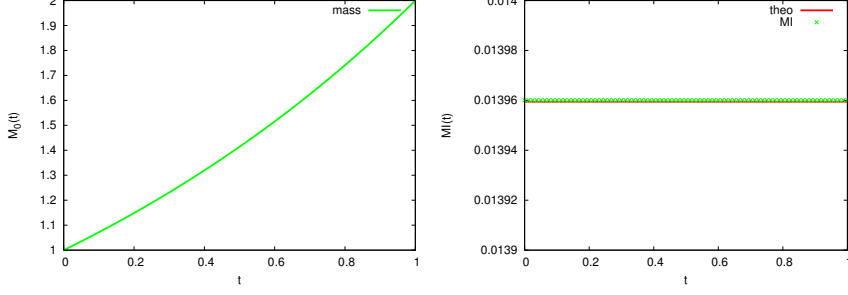


Figure 8: *Macroscopic outputs corresponding to the microscopic outputs of Figure 7: total cell number $m_f^0(t)$ (left panel) and mitotic index $MI(t)$ (right panel).*

where v_p is the (constant) velocity on the right of the interface and $v_{(p-1)}$ the velocity on its left, $k_p = 1$ in the case of flux continuity (interface G1-SM), while $k_p = 2$ in the case of flux doubling (interface SM-G1 phase where mitosis occurs). For the first interface (and starting the numbering of cell phases from 0),

$$\psi_1(t, x) = \begin{cases} \psi_0(x - v_0 t) & \text{for } x < x_s, \\ \tilde{\psi}_1(t_s) & \text{for } (x_s - v_1 t) \leq (x - v_1 t) < x_s, \\ \psi_0(x - v_1 t) & \text{for } (x - v_1 t) \geq x_s, \end{cases} \quad (44)$$

where $\tilde{\psi}_1$ is the trace of the solution on the right of the interface, defined by

$$\tilde{\psi}_1(t) = \frac{1}{v_1} k_1 (v_0 \psi_0(x_s - v_0 t)), \quad (45)$$

and t_s is the delay after which the effect of interface x_s is felt at position x and time t defined by

$$t_s = t - \frac{(x - x_s)}{v_1}. \quad (46)$$

We now show how the exact solution for a sequence of N_c cell cycles can be defined recursively. Let us denote by $\psi_{p-1}(t, x)$ the solution for a sequence of $p - 1$ interfaces, with $p > 1$ and add a p^{th} interface at px_s with a coefficient k_p for the transmission condition and a velocity v_p on the right hand side. For $x < px_s$ the effect of the p^{th} interface is not felt and the solution is $\psi_{p-1}(t, x)$. For $x \geq px_s$, depending on time t , the effect of the interface is felt or not. If $(x - px_s) < v_p t$, traces of the solution crossing the p^{th} interface are multiplied by the k_p coefficient and transported at velocity v_p . The effects of these events are felt at position x after a delay $(x - px_s)/v_p$. If $(x - px_s) > v_p t$, the effect of the p^{th} interface is not felt yet and the initial condition defined on $x > px_s$ is transported at velocity v_p . We eventually have

$$\psi_p(x, t) = \begin{cases} \psi_{p-1}(x, t) & \text{for } x < px_s, \\ \tilde{\psi}_p(t_s^p) & \text{for } (px_s - v_p t) \leq (x - v_p t) < px_s, \\ \psi_0(x - v_p t) & \text{for } x - v_p t \geq px_s, \end{cases} \quad (47)$$

where $\tilde{\psi}_p$ is the trace of the solution on the right of the p^{th} interface, defined by

$$\tilde{\psi}_p(t) = \begin{cases} \frac{1}{v_p} k_p v_{p-1} \psi_{p-1}(px_s, t) & \text{if } p > 1 \\ \frac{1}{v_p} k_p v_{p-1} \psi_0(x_s - v_{p-1}t) & \text{otherwise,} \end{cases} \quad (48)$$

and t_s^p is defined by

$$t_s^p = t - \frac{(x - px_s)}{v_p}. \quad (49)$$

We have computed numerically the master equation from this recursiveness approach, with $v_p = 1/2$ for odd p indexes and $v_p = 1$ for even p indexes to mimic the alternation between $G1$ and SM phases. To simplify we set $x_s = 1/2$ and $D_c = 1$. The solution is displayed in Figure 9. The density is displayed at initial time (left panel) and after one cell cycle (center panel) with a color code highlighting the discontinuity at $x_s = 0.5$. The right panel displays the time evolution of macroscopic outputs (total cell number and mitotic index) in the case when the solution is computed from the recursiveness formula (47) (green lines) or from the Finite Volume method (blue lines). The lines are almost superimposed, which highlights the very good accuracy of the Finite-Volume numerical approximation.

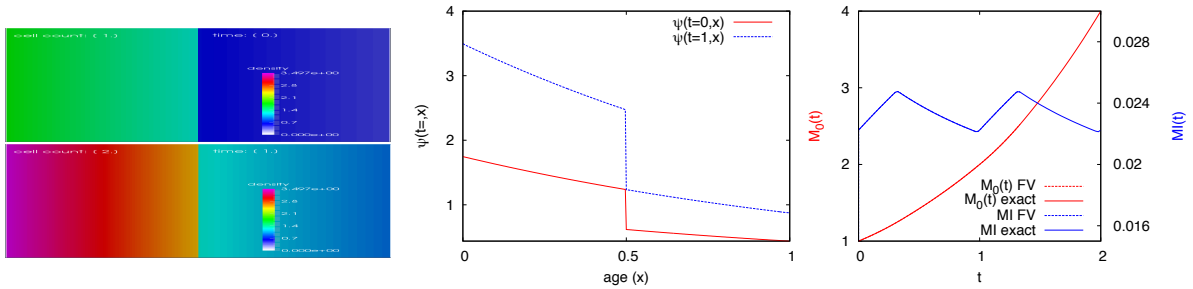


Figure 9: *Left panel: snapshots of the cell density $\phi(t, x, y)$ over the 2D domain (color-code panels) in the case of a fully proliferating, desynchronized cell population, with velocity contrast between the $G1$ ($g = 0.5$) and SM ($g = 1$) phases, at $t = 0.0$ (top) and $t = 1$ (bottom). Notice the discontinuity in the initial age distribution coming from (40). Center panel: age density $\psi(t, x)$ at $t = 0$ and $t = 1$. The shape of the density is periodically recovered after one cell cycle, and the cell number has doubled. Right panel: macroscopic outputs, total cell number (red) and mitotic index (blue). The dashed lines (computed from the Finite Volume method) and the solid lines computed from the recursiveness formula (47) are superimposed.*

A.3 Microscopic and macroscopic outputs in the case of cell cycle exit induced by differentiation and/or apoptosis

In our multiscale model, there is not only a contrast in the velocities according to the phases of the cell cycles, but also, due to the control terms, the velocities are time-varying. Moreover, cells are subject both to differentiation and apoptosis in phase $G1$,

which affects the age distribution of cells within the cell cycle, hence the kinetics indexes such as MI and GF.

In this section, we design the simplest setup that can account for these facts and can help illustrate the changes observed in the model outputs, without coping yet with the full complexity of the model. To this end, we have to consider the genuine 2D character of the model, and introduce the time-varying and maturity-dependent expression for h_f , as defined in (4), and we need to deal with the source term and the apoptosis rate formulated in (6), but we can bypass the closed-loop definition of $U(t)$ in (8), to impose instead a simple open-loop time pattern to $U(t)$. In addition, we forget about the distinction between $U(t)$ and the local control $u_f(t)$. More precisely, we consider the following function of time:

$$u_f(t) = U(t) = U^{ol} := \begin{cases} U_{\max}, & \text{for } t \leq T_s \\ U_{\min}, & \text{for } > T_s \end{cases} . \quad (50)$$

Also, in this setup, the parameter values are not intended to take realistic values (i.e. values that would lead to model outputs meeting the quantitative biological specifications), but they are chosen so that a complete cell cycle exit can occur rapidly and be observed as soon as after 2 cell cycles have elapsed. The aging velocity is kept unchanged with respect to the former subsections, as a piecewise constant function with $g \neq 1$ in phase G1 and $g = 1$ in SM.

The initial condition (2) is now uniformly spread over the initial maturity range $[\mu_1, \mu_2]$

$$\phi_0(x, y) = \frac{1}{\mu_2 - \mu_1} \psi_0(x) \mathbb{1}_{[s_1, s_2]}(y) \quad (51)$$

where ψ_0 is defined by (42).

We now comment a detailed simulation corresponding to this dynamical framework that has been designed to embed, as simply as possible, differentiation- or apoptosis-induced cell cycle exit, and to study its impact on the model outputs on different scales. The microscopic outputs for the $\phi(t, x, y)$ density are illustrated on Figure 10, where snapshots are shown at six different times. The computational domain is made of eight consecutive cycles, but for each snapshot, we only display the part of the computational domain containing the support of the density.

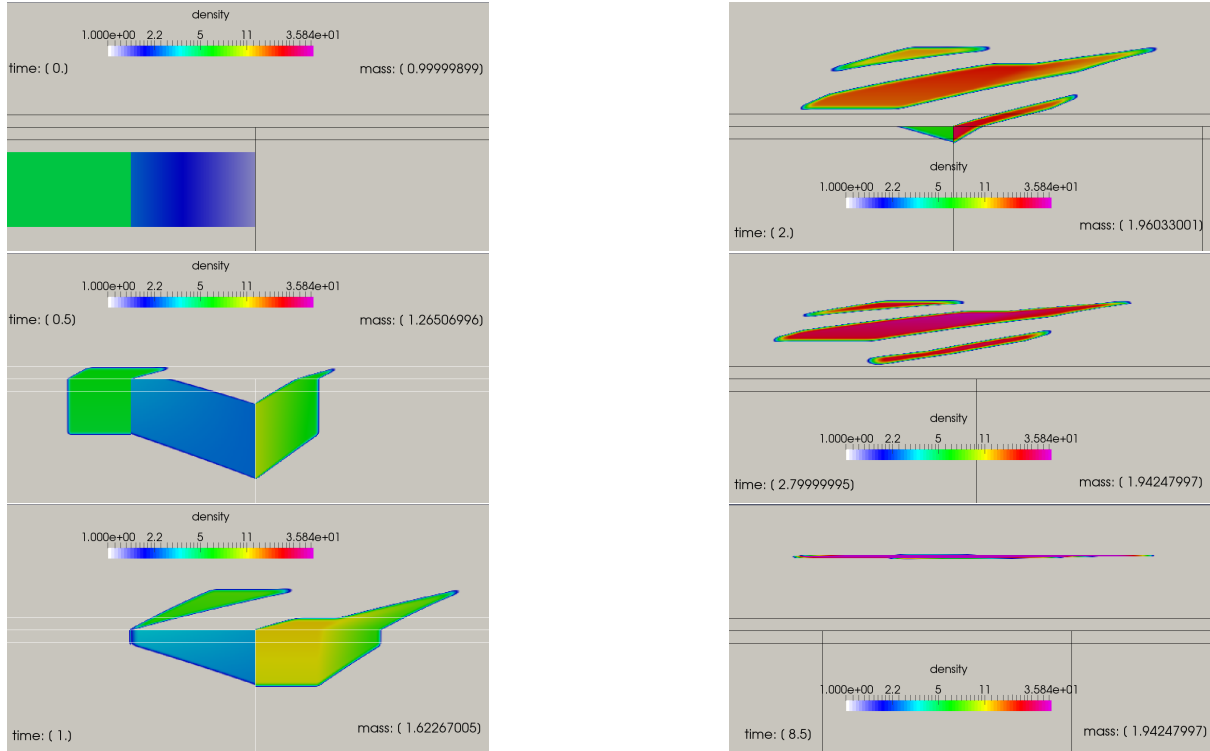


Figure 10: Snapshots of the cell density $\phi(t, x, y)$ over the 2D domain at $t = 0, 0.5, 1, 2, 2.7$ and 8.5 . Parameters are set to $\tau_h = 0.4$, $c_1 = 0.01$, $c_2 = 1.2$, $\bar{u} = 0.1$, $g = 0.5$ in G1 for the velocities, $U_{max} = 0.15$, $U_{min} = 0.075$ and $T_s = 2$ for the open-loop control and $\bar{\Lambda} = 0.2$, $\bar{y} = 0.1$ for the apoptosis rate. The same logarithmic color scale is used for all times, from 1 in white to 35.8 in pink. The three horizontal black lines on each snapshot materialize the thresholds $y_s^- = 0.45$, $y_s = 0.5$ and $y_s^+ = 0.55$. The same logarithmic color code is used for all snapshots. It is well suited to the exponential increase in the cell number and concentration of the density in the maturity direction. Sharp changes in color happen on the interfaces between phases, where velocity contrasts induce density discontinuities due to conditions (11), (12) and (13). The narrowing of the density support in phase D rather induces smooth changes in color, towards the highest color levels.

At initial time, the density is all contained within the first cell cycle and the maturity range is $[0.1, 0.4]$. At time $t = 0.5$, some cells have undergone mitosis and spread over the second cycle, while others are exiting the first cell cycle. At time $t = 1$, the density is splitting into two disconnected regions; some of the cells have already escaped from the apoptosis zone (their maturity overcomes the y_s^+ threshold in phase D). At time $t = 2$, the density has almost completely entered the upper phase of the domain and it is composed of three disconnected regions. The same is true at time $t = 2.8$, when all cells have not only exited the cell cycle, but also escaped from the apoptosis zone. The last snapshot, at time $t = 8.5$ illustrates the “contracting” property of the maturation function, that tends to pitch the density horizontally as the average maturity approaches the asymptotic value corresponding to the positive root (here $r_2(U_{min})$); this property has been theoretically established in [19] for a slightly different model where the distinction between SM and G1 phases is not made.

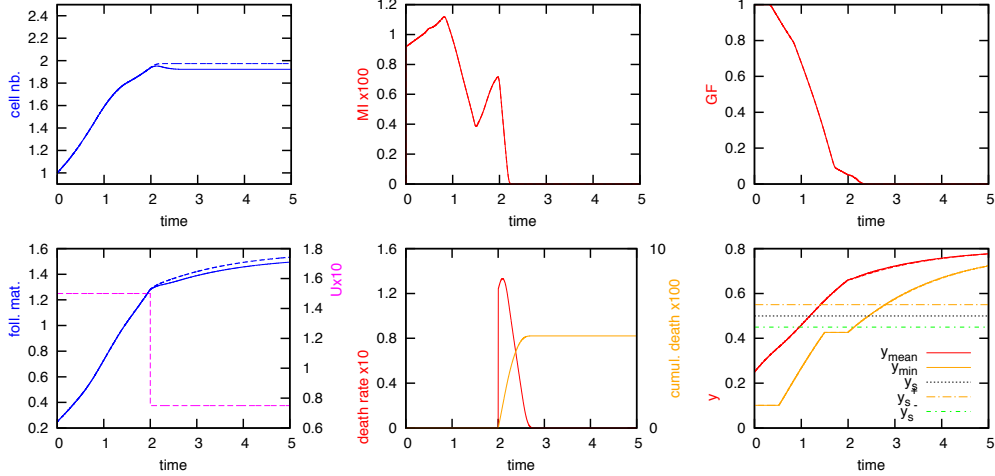


Figure 11: *Macroscopic outputs: total cell number (top left panel) ; mitotic index (top center panel) ; growth fraction (top right panel) ; piecewise constant control and follicular maturity (bottom left panel) ; instantaneous and cumulated cell death (bottom center panel); average (red solid line) and minimal (red dashed line) cell maturity (bottom right panel). In the left panels the solid line correspond to $\bar{\Lambda} = 1.6$ in the source term, the dashed line corresponds to $\bar{\Lambda} = 0$ (no apoptosis). The effect of apoptosis is hardly visible on the mesoscopic outputs.*

The macroscopic outputs are displayed on Figure 11. In addition to the total cell number (top left panel) and mitotic index (top center panel), the figure shows the decrease in the growth fraction (top right panel) due to cell cycle exit (GF was not shown in the former subsections since $GF = 1$ there) and the changes in the follicular maturity $m_1^1(t)$ (bottom left panel, which was neither shown up to now, because its time pattern superimposed on the total cell number). Also, to understand these macroscopic outputs in more depth, we introduce new mesoscopic indexes, such as (i) the changes in the minimum, average and maximum maturity (bottom right panel), and (ii) the instantaneous and cumulated cell death (bottom center panel). We also plot the changes in $U(t)$ according to (50), where $T_s = 2$ to condense all interesting events (and especially the triggering of apoptosis) in short time (the physiological drop would occur later, see next sections).

With the set of parameters chosen for this example, the total cell number stops increasing around $t = 2.11$. Before that time, the slope in the cell number increase had been lowered due to the intensification of cell differentiation. The growth fraction decreases steadily from its maximal value (1, since all cells are in the proliferative part of the domain at initial time) to a null value at the time when all cells have exited the cell cycle. This exit time (around $t = 2.33$) roughly coincides with the abscissa of the crossing point between the horizontal line delimiting the y_s threshold and the minimum maturity (red dashed line on the bottom right panel), even if numerical diffusion blurs a little the precise assessment of the coordinates of this crossing point. It is not exactly the same as that when the total cell number stabilizes, due to effect of apoptosis. A slowing-down in GF decrease can be seen between $t = 1.7$ and $t = 2.11$. This is due to a transient relative lowering of the denominator in (16) with respect to its numerator. After $t = 2.$, apoptosis is active and

is no more compensated by proliferation. Indeed the cell number even decreases a little before stabilizing around $t = 2.54$. The mitotic index first follows a pattern resembling that of Figure 9 with a sharply damped second peak, and then drops to zero at the exit time.

B Derivation of constraints for the aging and maturation velocities

Bounds of the parameters entering the g_f aging function Here we detail how we fix the bounds of the set Ω_g of admissible values for the γ_1 and γ_2 parameters in the aging velocity function g_f

$$\Omega_g \subsetneq [0, \gamma_{1\max}] \times [\gamma_{2\min}, g_{\max}]$$

Let us denote by $[u_{\min}, u_{\max}]$ the extremal values that may be taken by the local control u_f . In the open loop piecewise constant setup (20)

$$u_{\min} = b_1 U_{\max}, \quad u_{\max} = \max(b_2 U_{\max}, U_{\min}), \quad (52)$$

while in the closed loop original setup (8,9)

$$u_{\min} = b_1 U_{\min}, \quad u_{\max} = U_{\max}. \quad (53)$$

From the aging velocity and the length of the cell phases, we can derive the average duration of phases SM and G1

$$T_{SM} = \frac{D_c - x_s}{1}, \quad \text{and } T_{G1} = \frac{x_s}{g_f},$$

Denoting by $r\%$ the level of modulation operated by the hormonal control on the aging velocity, we get

$$\frac{T_{SM}}{T_{G1}}(1 - r) \leq g_{\min} < g_f(u_f(t)) < g_{\max} \leq 0.5(1 + r) \frac{T_{SM}}{T_{G1}} \quad (54)$$

In our specific case $D_c = 2x_s = 1$, so that $T_{SM}/T_{G1} = 1/2$, and we obtain the following inequality constraints for γ_1 and γ_2

$$g_{\min} \leq \gamma_1 u_{\min} + \gamma_2 \quad (55)$$

$$\gamma_1 u_{\max} + \gamma_2 \leq g_{\max} \quad (56)$$

so that

$$\gamma_{1\max} = \frac{g_{\max} - g_{\min}}{u_{\max} - u_{\min}} \quad \text{and} \quad \gamma_{2\min} = \frac{g_{\min} u_{\max} - g_{\max} u_{\min}}{u_{\max} - u_{\min}}. \quad (57)$$

Note that the bounds in (57) depend indirectly on the parameters of the b_f function, and more specifically on b_1 (and also β_2 in the open loop setup). In practice, we first select the pair (γ_1, γ_2) independently, and then check whether the selected values are compatible with all other constraints imposed on the whole parameter set. A practical domain for searching the pair is the minimal box containing $\cup_{b_1} \Omega_g(b_1)$, *i.e.* the bounds (57) evaluated at $b_1 = b_{1\max}$.

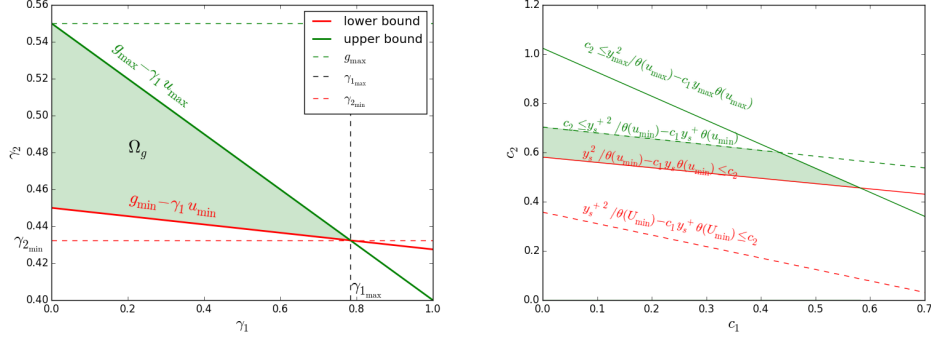


Figure 12: *Left panel* : admissible values for parameters γ_1 , γ_2 , satisfying constraints (56) ($g_{\min} = 0.45$, $g_{\max} = 0.55$, $b_1 = 0.3$, closed loop setup). *Right panel*: admissible values for parameters c_1 , c_2 , satisfying constraints (62). The polygon delimited by Ω_h lies above the red lines and below the green ones.

Bounds of the parameters entering the h_f maturation function We will now derive constraints on the bounds of the set Ω_h of admissible values for the c_1 and c_2 parameters in the maturation velocity function h_f

$$\Omega_h \subsetneq [0, c_{1\max}] \times [c_{2\min}, c_{2\max}] \quad (58)$$

The positive root of h_f , $r_2(u_f)$ is an increasing function of u_f . In the ovulatory case, the development of the follicle is well synchronized with the FSH environment (“right time - right place”), so that it is able to take advantage of even low level of FSH (U_{\min}) and

$$\begin{aligned} y_s &\leq r_2(u_{\min}) \\ r_2(u_{\max}) &< y_{\max}. \end{aligned} \quad (59)$$

along with

$$y_s^+ \leq r_2(U_{\min}). \quad (60)$$

Yet, if the follicle fails to adapt to low FSH levels [15], ($b_f \leq 1$ when $U = U_{\min}$), then, as in the atretic case, the cells can be trapped in the part of the differentiated domain where they are sensitive to apoptosis in case of an unfavorable FSH environment (typically when $U(t) = b_1 U_{\min}$) and

$$y_s \leq r_2(b_1 U_{\min}) \leq y_s^+ \quad (61)$$

Similarly to Ω_g , the bounds of Ω_h depend indirectly on the parameters of the b_f function, b_1 and \bar{u} (as well as b_2 in the open loop setup). As can be seen on the right panel of Figure 12, Ω_h is a polygon bounded by the following lines, derived from (59,60,61)

$$\begin{aligned} y_s^2 / \theta(u_{\min}) - c_1 y_s \theta(u_{\min}) &\leq c_2 \\ c_2 &\leq y_{\max}^2 / \theta(u_{\max}) - c_1 y_{\max} \theta(u_{\max}) \\ y_s^{+2} / \theta(U_{\min}) - c_1 y_s^+ \theta(U_{\min}) &\leq c_2 \leq y_s^{+2} / \theta(u_{\min}) - c_1 y_s^+ \theta(u_{\min}) \end{aligned} \quad (62)$$

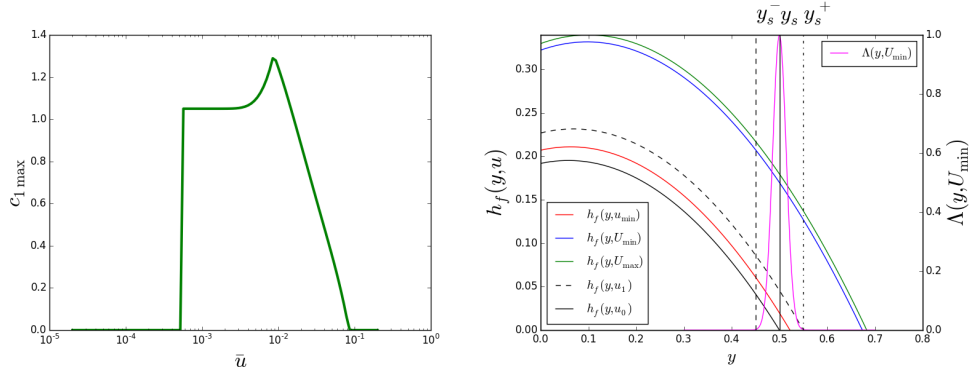


Figure 13: *Left panel: sketch of non emptiness criterium (63). Maximum bound for c_1 parameter as a function of \bar{u} . Right panel: $h_f(y, u)$ and $\Lambda(y, U_{\max})$ versus y for $c_1 = 0.2$, $c_2 = 0.5$, $\bar{y} = 0.02$, $u = U_{\max}$ (green line), $u = U_{\min}$ (blue line), $u = u_{\min}$ (red), $u = u_0$, with $r_2(u_0) = y_s$ (black solid line) and $u = u_1$, with $r_2(u_1) = y_s^+$ (black dashed line).*

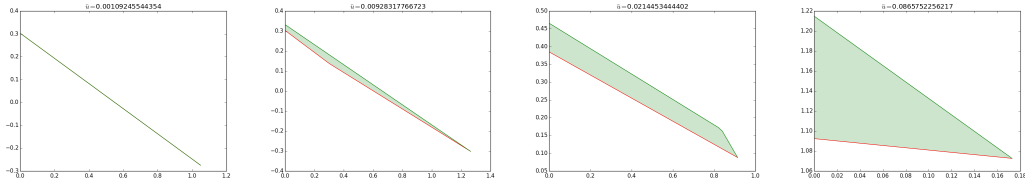


Figure 14: *Admissible sets (c_1, c_2) for varying values of \bar{u} (from left to right 0.001, 0.009, 0.021, 0.086).*

The combinations of c_1 and c_2 that fall within the polygon area are not arbitrary and we can derive a condition preventing from emptiness of Ω_h

$$\max \left(\frac{y_s^{+2}}{\theta(U_{\min})}, \frac{y_s^2}{\theta(u_{\min})} \right) \leq \min \left(\frac{y_s^{+2}}{\theta(u_{\min})}, \frac{y_{\max}^2}{\theta(u_{\max})} \right)$$

When the condition is met

$$\Omega_h \subsetneq [0, c_{1\max}] \times \mathbb{R},$$

with

$$c_{1\max} = \max \left(0, \min \left(\frac{\frac{y_{\max}^2}{\theta(u_{\max})} - \frac{y_s^2}{\theta(u_{\min})}}{y_{\max}\theta(u_{\max}) - y_s\theta(u_{\min})}, \frac{y_s^+ + y_s}{\theta(u_{\min})^2} \right) \right) \quad (63)$$

The existence of non-empty sets is illustrated as a function of parameters \bar{u} and c_1 in the left panel of Figure 13.

Once we are guaranteed that $c_1 \in [0, c_{1\max}]$, we deduce that

$$c_{2\min} = \max \left(\frac{u_s^{+2}}{\theta(U_{\min})} - c_1 y_s^+ \theta(U_{\min}), \frac{y_s^2}{\theta(u_{\min})} - c_1 y_s \theta(u_{\min}) \right),$$

$$c_{2\max} = \min \left(\frac{u_s^{+2}}{\theta(u_{\min})} - c_1 y_s^+ \theta(u_{\min}), \frac{y_{\max}^2}{\theta(u_{\max})} - c_1 y_{\max} \theta(u_{\max}) \right).$$

The shape and area of different admissible sets corresponding to different values of \bar{u} are depicted in Figure 14, while Figure 13 gives an instance of the resulting graph of $h_f(y, u)$ versus y after applying the strategy for finding a specific parameter set belonging to Ω_h .

Additional comments on the hypotheses underlying the choice of $\Lambda(y, U)$ The formulation of the cell loss intensity transcribes on the cell level what is well established on the follicle level. Indeed, the vulnerability of a follicle to atresia (follicle degeneration) is maximal at the time of selection of future ovulatory follicles (follicles of 3-4mm in ewes [20]), which is also the time when the drop in the growth fraction is the highest. Before the selection time, this vulnerability appears at the moment of the switch from a FSH-responsive to a FSH-dependent stage (follicles of 2,5mm in ewes [26]), while it disappears when the follicle is selected (dominant follicle) and able to switch its dependence from FSH to LH. Since follicle atresia is mediated by granulosa cell apoptosis, it seems quite natural to draw an equivalence between the cell sensitivity to apoptosis and the follicle dependence towards FSH, and between, respectively, (i) the exit time (where $y = y_s$) and the selection time, (ii) the time when the cell reaches y_s^- and the time of FSH-dependency triggering and (iii) the time when the cell overcomes y_s^+ and the time of dominance. The shape of Λ is displayed in the right panel of Figure 13.

C Optimization steps using CMAES and flow charts for the whole procedure of parameter calibration

C.1 Identification of a single ovulatory trajectory

In this paragraph, we make use of the piecewise constant, open-loop caricature of the nonlocal control $u_f^{ol}(t)$, introduced in section 3 of the main text, to derive an initial guess for a parameter set of an ovulatory trajectory. We follow a simple strategy that consists in taking as *a priori* observations the moments corresponding to the first switching time and exit time and estimating the values of the parameters in the h_{ov} , g_{ov} and u_{ov}^{ol} functions from a multi-objective optimization step using the stochastic algorithm CMAES [12]. The set of parameters is

$$\{p = (b_1, \beta_2, \tau_h, \bar{u}, T_{s_2}, c_1, c_2, \gamma_1, \gamma_2) \in \Omega_p\},$$

with Ω_p a polygon (described in Appendix B) taking into account constraints on the velocities h_{ov} and g_{ov} , while the criterion reads

$$J_{ol}(p) = \sum_{i=1}^4 \alpha_i f_i(p), \quad (64)$$

with

$$f_1(p) = |T_{s_1} - T_{s_1}^{exp}|^2, \quad f_2(p) = |T_e - T_e^{exp}|^2, \quad (65)$$

$$f_3(p) = |m_{ov}^0(T_{s_1}) - m_{s_1}^{exp}|^2, \quad f_4(p) = |m_{ov}^0(T_e) - m_e^{exp}|^2. \quad (66)$$

T_{s_1} coincides with the onset of FSH-dependency (delimited by green dashed lines on Figure 4 in the main text) and $m_{s_1}^{exp}$ is the corresponding cell number observed at T_{s_1} (≈ 3.16), while T_e^{exp} corresponds to the exit time (delimited by black dashed lines on Figure 4) and m_e^{exp} is the corresponding cell number observed at T_e^{exp} (≈ 6.7). Weights α_i , $i = 1, \dots, 4$ are fitted numerically.

In the open-loop framework, the cell number $m_{ov}^0(T_{s_1})$ and $m_{ov}^0(T_e)$ can be roughly computed from the simplifying expression (35). This is of course a crude estimation of the evolution in time of the cell number, since it amounts to dealing with the population as if it was fully proliferating and with a point initial distribution in maturity, but it leads nevertheless to quite satisfactory results for a first trial.

Next, starting from the initial guess p^* (see Table 2) retrieved from the particle-based calibration, we proceed to the direct comparison of the simulated outputs, obtained by simulating the 2D PDE model in the open-loop framework, with the observed cell numbers, and perform a classical, CMAES-based optimization with a single objective criterion:

$$J_c(p; q) = \sum_{i=1}^n |m_{ov}^0(t_i) - m^{exp}(t_i)|^2, \quad (67)$$

where t_i corresponds to the sampling times and $m^{exp}(t_i)$ to the observed cell number at each time (whole set of red crosses on Figure 4), with the set of estimated parameters

$$p = (\gamma_1, \gamma_2, \tau_h),$$

where γ_1 and γ_2 must belong to the set $\Omega_g(b_1)$ defined in Appendix B while the parameters

$$q = (b_1, \beta_2, \bar{u}, T_{s_2}, c_1, c_2)$$

are kept equal to their values in p^* .

Going back to the full, closed-loop formulation of the model, we can draw some equivalence with the open-loop case to fix starting values for the parameters of the $S(M)$ (eq. 8) and b_{ov} (eq. 9) functions. We thus deduce the starting value of $b_3 = 6.9$ from the ovarian maturity reached at $T_{s_1} = 4.3$ (green dashed lines on the top center panel in Figure 5) and that of $\bar{M} = 13.3$ from the maturity at T_{s_2} (blue dashed lines on the same panel). Keeping unchanged the values of parameters $q = (b_1, c_1, c_2, \bar{u})$ from their values in \hat{p} , we search for the parameters $\{p = (b_2, b_3, \tau_h, \gamma_1, \gamma_2, \bar{M}, c, \bar{\Lambda}) \in \Omega_p\}$ using an augmented version of criterion (67):

$$J_{cc}(p; q) = J_c(p; q) + C_{ov}(p; q), \quad (68)$$

with

$$C_{ov}(p; q) = (U(T_e) - U_{\min}) + \max(0, R_{ov}(T_e) - \alpha_R m_{ov}^0(T_e)). \quad (69)$$

The first term in the penalization criterion (69) ensures that the single follicle evolves in a realistic hormonal environment (including the drop in FSH levels), while the second term controls the loss by apoptosis. Even if apoptosis is a physiological process occurring also in healthy follicles, its incidence is much lower (an order of magnitude of tenfold) in ovulatory follicles than in atretic ones [16], and we can roughly consider that the cumulated cell loss does not exceed $\alpha_R = 10\%$ of the cell number at ovulation time.

C.2 Calibration of interacting ovulatory and atretic trajectories

We finally dispose of a reasonable parameter set p_{ov} (see values in Table 2, and solid black lines in top panels of Figure 5) for a closed-loop ovulatory trajectory that we now intend to couple with another trajectory corresponding to an atretic follicle. Letting the local parameters of p_{ov} unchanged, we search for another follicle-specific set

$$p_{atr} = (b_1, b_2, b_3, \tau_h, c_1, c_2, \bar{u}, \gamma_1, \gamma_2, \bar{M}, c, \bar{\Lambda})$$

that should meet two types of constraints. As in the ovulatory case, we first select a set of admissible parameters $q = (b_1, \bar{u}, c_1, c_2)$ as defined in Appendix B. In contrast to the ovulatory situation, we do not dispose of direct experimental datasets on cell numbers to which we could fit the macroscopic outputs of the model. However, we can derive a penalization criterion that constrains the trajectory of atretic follicles with respect to the ovulatory trajectory, basing ourselves on the range of cell number values observed at a given development stage in a population of growing follicles (see the data cloud on Text-fig 1 in [32]). We expect at the same time that

1. the cell number increases significantly with respect to its initial value up to the selection time,
2. the increase in the cell number remains moderate,

3. the cell loss becomes substantial after this time, with a final cell number clearly lower than the maximal number reached along the atretic trajectory.

Denoting by m_f^* the maximum cell number reached by follicle f over the time window we express these requirements within a multi-criterion function

$$C_{atr}(p; q) = \nu_1 |\theta_1 - m_{atr}^*|^+ + \nu_2 |m_{atr}^* - \theta_2|^+ + \nu_3 \frac{|m_{atr}^0(t_f) - \theta_3 m_{atr}^*|^+}{m_{atr}^*}, \quad (70)$$

where θ_1 (respectively θ_2) is the minimum (resp. maximum) cell number value below (resp. beyond) which the computed cell number contributes to the fit function, while θ_3 measures cell loss due to atresia. Weights ν_1, ν_2 and ν_3 are fitted numerically. At the same time, the new atretic trajectory should be still compatible with the ovulatory behavior of the other follicle, which is ensured by the constraint C_{ov} . We therefore seek a minimum of

$$J_{atr}(p; q) = C_{atr}(p; q) + C_{ov}(p; q), \quad (71)$$

where $\{p = (b_2, b_3, \tau_h, \gamma_1, \gamma_2, \bar{M}, c, \bar{\Lambda}) \in \Omega_{pf}\}$, in which the first five (local) parameters correspond to the atretic follicle. For this last stage the thirteen other parameters

$$q = (b_1^{ov}, b_2^{ov}, b_3^{ov}, \tau_h^{ov}, c_1^{ov}, c_2^{ov}, \bar{u}^{ov}, \gamma_1^{ov}, \gamma_2^{ov}, b_1^{atr}, \bar{u}^{atr}, c_1^{atr}, c_2^{atr})$$

are kept constant.

C.3 Flow charts for parameter identification

We now summarize the different identification steps leading to the final set of parameters p_{ov} and p_{atr} in Table 2. We follow a sequential procedure that involves the successive CMAES-based optimization of the four criteria J_{ol} , J_c , J_{cc} , J_{atr} (Step 1, 2, 3 and 5 in Figure 15), whose main steps are summarized in Figure 16. Depending on the size of the parameter set entering the optimization procedure, the dimension of the parameter space vary between 3 (in the case of \hat{p}) and 9 (in the case of p^*). Fortunately, the search for p^* does not require the simulation of the PDE model since it is only based on the computation of the characteristic times. Hence, although only few *a priori* bounds on the 9 unknown parameter values are provided in this case, the computational cost associated with the assessment of J_{ol} remains largely tractable[†]. In contrast, Steps 2, 3 and 5 do need to perform numerical simulations of the PDEs, from the finite volume numerical method described in [4, 5], with $N_x \times N_y = 40^2$ grid points per cycle and CFL= 0.4. Besides the optimization steps, Step 4 is needed to select admissible values for parameters of atretic follicles (b_1, c_1, c_2, \bar{u}) as described in Appendix B, before the assessment of J_{atr} in Step 5.

[†]If we merge weights $(\alpha_i)_{i=1,\dots,4}$ with the set of unknown parameters, the solution found by CMAES is a weak Pareto minimum favoring only the first objective (good coincidence in time between the theoretical value of T_{s1} and its observed value). In contrast, if we arbitrarily impose $\alpha_i = 1$ for all $i = 1, \dots, 4$ the fit is much more balanced over the four objectives. Similarly we set $\nu_1 = 10, \nu_2 = 1, \nu_3 = 20, \theta_1 = 25, \theta_2 = 30$ and $\theta_3 = 0.5$ in (70) to obtain the parameters p_{atr} .

Param	p^*	\hat{p}		p_{ov}	p_{atr}
γ_1	0.249	0.0626		0.1	0.010
γ_2	0.745	0.479		0.45	0.548
c_1	0.130	0.130		0.130	0.015
c_2	0.311	0.311		0.311	0.295
\bar{u}	0.0145	0.0145		0.0145	0.0123
τ_h	0.305	0.31		0.28	0.522
b_1	0.249	0.249		0.249	0.287
β_2	0.717	0.717	b_2	0.8	0.973
T_{s1}	4.3	4.3	b_3	6.	14.563
T_{s2}	6.	6.	\bar{M}	14.	24.
T_e	8.	8.	c	0.7	0.3
			δ	1.	2.
Λ				0.	0.5

Table 2: Parameter values for the different parameter sets introduced in section C.1 and C.2. Parameters with fixed nominal values are $\bar{y} = 0.02$, $M_0 = 1$, $g_{\min} = 0.45$, and $g_{\max} = 0.55$, as well as those in Table 1. p^* is obtained from the particle-derived criterion J_{ol} . \hat{p} is obtained from criterion (67) and requires the simulation of the PDE model in the open loop setup. \hat{p} is used to obtain the preliminary fitted cell numbers shown on the rightmost top panel of Figure 5. p_{ov} and p_{atr} are the final outputs of the whole estimation procedure. For p_{ov} , the bounds on the aging velocity parameters γ_1 and γ_2 are set using (57). For p_{atr} , the admissible initial guess is obtained from constraint (62), as described in Appendix B. The values highlighted in color (blue or green) are the result of the current optimization set, while those left in black are inherited from the previous steps. To obtain the whole set of parameters, one just need to concatenate the values in column p_{atr} with the first nine rows in column p_{ov} (all values except those highlighted in green).

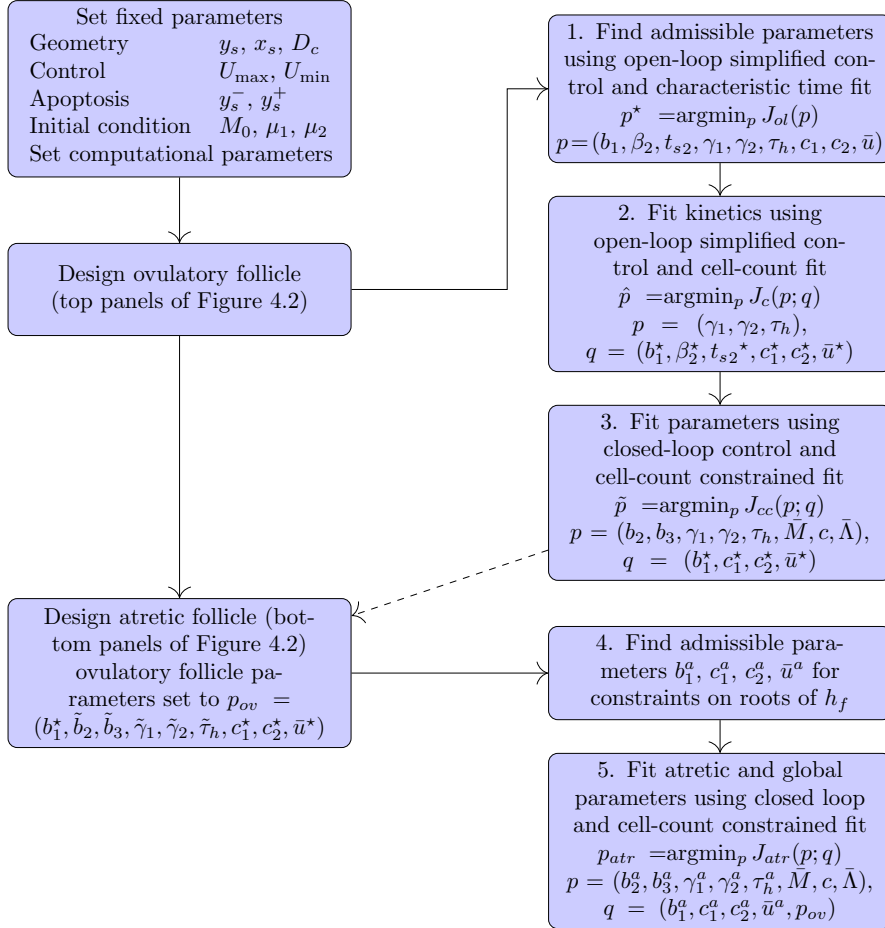


Figure 15: Flow chart for parameter identification. In steps 2, 3 and 5, the whole parameter set is subdivided into set q , whose values were obtained from the previous optimization steps (respectively 1, 2 and 3) and are left unchanged, and set p , that is subject to the current optimization procedure.

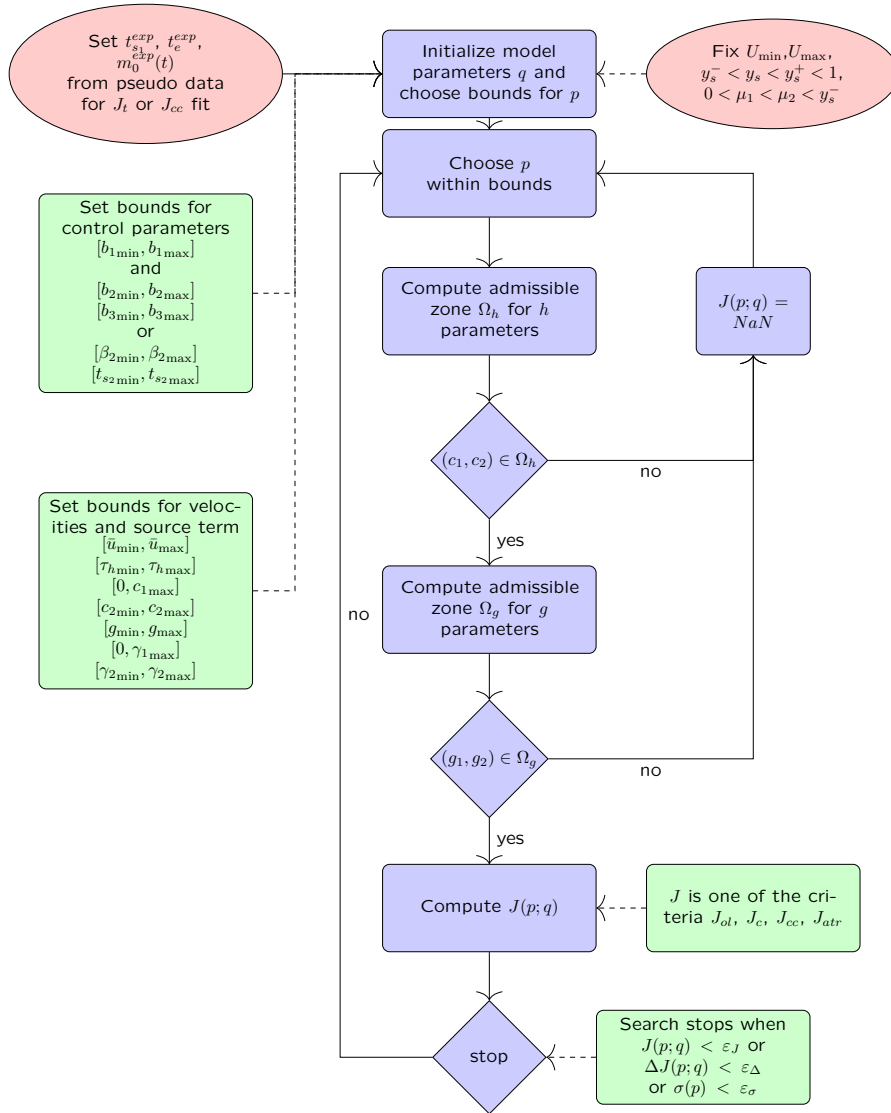


Figure 16: Flow chart for the CMAES-based optimization of criteria (64,67,68,71). The Python library *cma* was used to find the parameter values corresponding to local minima of the criterion.